Experimental characterization of the agitation generated by bubbles rising at high Reynolds number

G U I L L A U M E   R I B O U X[1,2], F R É D É R I C   R I S S O[1,2]†
A N D   D O M I N I Q U E   L E G E N D R E[1,2]

[1]Université de Toulouse; INPT, UPS; IMFT (Institut de Mécanique des Fluides de Toulouse);
Allée Camille Soula, F-31400 Toulouse, France

[2]CNRS; IMFT; F-31400 Toulouse, France

An experimental investigation of the flow generated by a homogeneous population of bubbles rising in water is reported for three different bubble diameters ($d = 1.6$, 2.1 and 2.5 mm) and moderate gas volume fractions ($0.005 \leqslant \alpha \leqslant 0.1$). The Reynolds numbers, $Re = V_0 d / \nu$, based on the rise velocity V_0 of a single bubble range between 500 and 800. Velocity statistics of both the bubbles and the liquid phase are determined within the homogeneous bubble swarm by means of optical probes and laser Doppler anemometry. Also, the decaying agitation that takes place in the liquid just after the passage of the bubble swarm is investigated from high-speed particle image velocimetry measurements. Concerning the bubbles, the average velocity is found to evolve as $V_0 \alpha^{-0.1}$ whereas the velocity fluctuations are observed to be almost independent of α. Concerning the liquid fluctuations, the probability density functions adopt a self-similar behaviour when the gas volume fraction is varied, the characteristic velocity scaling as $V_0 \alpha^{0.4}$. The spectra of horizontal and vertical liquid velocity fluctuations are obtained with a resolution of 0.6 mm. The integral length scale Λ is found to be proportional to V_0^2 / g or equivalently to d / C_{d0}, where g is the gravity acceleration and C_{d0} the drag coefficient of a single rising bubble. Normalized by using Λ, the spectra are independent on both the bubble diameter and the volume fraction. At large scales, the spectral energy density evolves as the power -3 of the wavenumber. This range starts approximately from Λ and is followed for scales smaller than $\Lambda/4$ by a classic $-5/3$ power law. Although the Kolmogorov microscale is smaller than the measurement resolution, the dissipation rate is however obtained from the decay of the kinetic energy after the passage of the bubbles. It is found to scale as $\alpha^{0.9} V_0^3 / \Lambda$. The major characteristics of the agitation are thus expressed as functions of the characteristics of a single rising bubble. Altogether, these results provide a rather complete description of the bubble-induced turbulence.

Key words: bubble dynamics, gas/liquid flows, turbulent flows

---

1. Introduction

In many practical situations, bubbles are dispersed in a continuous liquid phase: pipe flow for oil transport, bubble columns for chemical processing, vapour generators

† Email address for correspondence: risso@imft.fr

for energy production. Due to the large density difference between gases and liquids, the bubbles do not move at the same velocity as the liquid. The bubbles thus cause velocity disturbances to the liquid that collectively generate a complex agitation. However, this bubble-induced agitation – also called pseudo-turbulence – is often not the only cause of liquid agitation. When the liquid flow is already turbulent in the absence of the bubbles, the overall agitation results from the two-way coupling between classic shear-induced turbulence and bubble-induced agitation. It therefore depends on the structure of these two kinds of agitation and, in particular, on their relative magnitudes and characteristic scales of time and length. The knowledge of pure bubble-induced agitation – that is to say in absence of shear-induced turbulence – is nevertheless required prior to understand this coupling.

An essential ingredient in bubble-induced agitation is the nature of the decay of the velocity disturbance U generated by a bubble with the distance r to this bubble. For an isolated bubble of diameter d moving at velocity V in a fluid of viscosity ν, this decay depends on the Reynods number, $Re = Vd/\nu$. At vanishing Re, the Stokes solution shows that the disturbance decays as r^{-1}. Because of this slow decay, the summation of the flow disturbances generated by a homogeneously distributed swarm of bubbles leads to the divergence of the variance of the fluctuations with the size of the container (Calfish & Luke 1985). At any finite Re, a wake develops behind the bubble wherein the disturbance again decays as r^{-1}; the linear summation of all individual bubble contributions therefore also leads to the divergence of the variance (Parthasarathy & Faeth 1990). At moderate-to-large Re, the non-divergence of the velocity variance is due to the fact that wakes of interacting bubbles are attenuated compared to that of an isolated bubble. For $1 < Re < 10$, Koch (1993) proposed a screening mechanism due to a deficit of particles in the wake of a test particle, which caused the disappearance of the wake disturbance at a distance that depends on the gas volume fraction α and scales as $d\alpha^{-1}$. Experimental evidence of wake attenuation related to a deficit of bubbles in the wake of a test bubble was found by Cartellier & Rivière (2001) in uniform bubbly flows for Reynolds numbers of order 10. At large Reynolds numbers, a non-uniform distribution of the bubbles is however not required to observe wake attenuation. Hunt & Eames (2002) showed that sequences of positive and negative strains might cause diffusion and cancellation of vorticity leading to wake attenuation. Another possible mechanism is the mixing of vorticity components of opposite signs belonging to neighbour wakes, which can make themselves disappear rapidly. White & Nepf (2003) and Eames *et al.* (2004) modelled this mechanism for a random array of bodies in a uniform flows and found an exponential wake attenuation with a length scale proportional to $dC_d^{-1}\alpha^{-1}$, where C_d is the drag coefficient of a body. Experimental evidence of such an exponential attenuation was observed in bubbly flows by Risso *et al.* (2008) for Reynolds numbers of several hundreds. However, although the length scale was indeed proportional to dC_d^{-1}, it was found independent of the gas volume fraction for $0.01 \leqslant \alpha \leqslant 0.14$. In this work, we shall focus on this regime for which the liquid agitation essentially results from nonlinear interactions between bubble wakes.

Ensuring that bubble-induced turbulence is the major contribution to the agitation in bubbly flows imposes very restrictive experimental conditions. A first way to achieve this goal is to inject bubbles in a upward flow within a channel, the width of which is large enough to allow the existence of an adequate central part where the liquid flow is uniform. The advantage of this configuration is that the use of hot-wire velocimetry is possible thanks to the existence of a significant average liquid velocity. The inconvenient is that turbulence generated at the wall is also present.

Such a configuration was used in the pioneering work devoted to the structure of high-Reynolds-number bubble-induced agitation by Lance & Bataille (1991). Theses authors added a grid at the channel inlet to control the properties of the incoming turbulence and studied the interaction between bubble-induced agitation and shear-induced turbulence. But since they considered large bubbles ($d = 5\,\text{mm}$), the bubble-induced agitation was predominant at moderate gas volume fractions. Comparable experimental set-ups, but without initial grid, were then considered by Garnier, Lance & Marié (2002) and in the PhD work of Larue de Tournemine (2001), which has been partly published in Roig & Larue de Tournemine (2007).

Another possible configuration is the bubble column, where bubbles are injected at the bottom of a tank filled with a liquid initially at rest and leave it from the free surface located at the top. Since the only cause of motions is the buoyancy-driven rise of the bubbles, this configuration seems the best choice for the study of the specific properties of the bubble-induced turbulence. It is however not so easy because most bubble columns are unstable, which means that large recirculation loops develop, the liquid generally rising close to the channel centre and descending close to the wall. In this case, shear-induced turbulence is also generated, especially at the walls. It is only when a particular care is taken to inject the bubbles uniformly at the tank bottom that a homogeneous swarm of bubbles without any average liquid flow can be generated for significant gas volume fractions (from several per cents to several tens of per cents). Bubble-induced turbulence in such a stable bubble column has been investigated by Zenit, Koch & Sangani (2001), Risso & Ellingsen (2002) and Martinez-Mercado, Palacios-Morales & Zenit (2007). Zenit *et al.* (2001) considered bubbles of $d = 1.4\,\text{mm}$ rising in water. This case was chosen to ensure a large Reynolds number concurrently to a small enough Weber number, with the aim to check the predictions of potential flow theory that required negligible bubble wakes. The use of a hot wire allowed the measurement of the liquid velocity variance for volume fractions up to 0.17, but prevented the separation of vertical and horizontal components of the fluctuations because of the lack of an average liquid velocity. On the other hand, Risso & Ellingsen (2002) considered high-Reynolds-number ellipsoidal bubbles of $d = 2.5\,\text{mm}$ rising in water. By using laser Doppler anemometry (LDA), they provided a detailed description of the liquid fluctuations, however restricted to gas volume fractions less than 0.01. More recently, Martinez-Mercado *et al.* (2007) used solutions of glycerin and water to vary the liquid viscosity and investigated the effect of the Reynolds number in the range $10 \leqslant Re \leqslant 500$, and they used a smart flying hot-wire technique to overcome the drawbacks of hot wire in the absence of mean flow. It is important to remark that, in all the investigations mentioned above, the populations of bubbles are approximately monodisperse, which allows to discuss the role of the bubble diameter. Except in the case of Lance & Bataille (1991), the bubbles were generated by using a regular array of capillary tubes.

The description of high-Reynolds-number bubbly flow involves the dynamics of both the bubbles and the liquid. Concerning the dispersed phase, all studies show that the mean velocity of the bubble $\langle V \rangle$ is a decreasing function of α. This decrease is attributed to the hindrance effect that corresponds to the fact that a backward flux of liquid has to develop in the interstitial flow between the bubbles to balance the volume of liquid that is entrained in the bubble vicinity. There is no general model for this phenomenon and the results of Martinez-Mercado *et al.* (2007) indicate that it is likely to depend on both the flow regime (Reynolds number) and the bubble shape (Weber number). Moreover, even for a given set of these parameters, several regimes have to be distinguished depending on α. In particular, the value of $\langle V \rangle$ measured for

the lowest volume fraction available in the experiments (a few tenths of a percent) is systematically lower than the value V_0 corresponding to the single rising bubble. The hindrance mechanisms then require a minimum volume fraction to develop. Also, Roig & Larue de Tournemine (2007) showed that, although taking into account the potential flows around the bubbles was sufficient to predict $\langle V \rangle$ for $\alpha < 0.02$, the liquid flux entrained in the wake became predominant for larger α. Then, for large volume fractions ($0.1 \leqslant \alpha \leqslant 0.3$), Garnier *et al.* (2002) observed that $\langle V \rangle$ scaled as $\alpha^{1/3}$. On the other hand, the fluctuations of the bubble velocity follow a totally different trend than the average velocity. At low volume fractions ($0.005 \leqslant \alpha \leqslant 0.01$), Risso & Ellingsen (2002) found that the bubble agitation was similar to that of a single rising bubble and was thus driven by the vortex shedding that occurred in the wake. Martinez-Mercado *et al.* (2007) then showed that the variance of the bubble velocity remained almost constant for volume fractions up to at least 0.1. The bubble agitation thus appears to depend neither on the bubble rise velocity nor on the liquid dynamics, which both depend on α.

Concerning the liquid agitation, Risso & Ellingsen (2002) showed that the probability density functions (PDFs) of the velocity fluctuations were independent of the gas volume fraction, provided the velocity was normalized by $V_0\alpha^{0.4}$. This self-similar behaviour, originally obtained for $0.005 \leqslant \alpha \leqslant 0.01$ and $Re = 800$ was confirmed by Martinez-Mercado *et al.* (2007) to hold for volume fractions up to 0.1 and Reynolds numbers from 10 to 500. Another important feature of the liquid agitation is the spectral distribution of the fluctuating energy with the wavenumber k. In the context of bubbly flows, Lance & Bataille (1991) were the first to find a spectral density of energy evolving as $k^{-8/3}$ and to claim that it was the signature of the bubble-induced turbulence. Then, depending on the bubbly flow that was investigated, a range of wavenumbers with an exponent close to -3 was observed or not (see Rensen, Luther & Lohse 2005, for a detailed review). The comparisons between the different works is complicated for two reasons. The first reason is that the spectra are generally computed from signals which are interpolated during the intervals when bubbles are present at the measuring point; the exponent of the spectra may therefore depend on the interpolation method that is used. The second reason arises from the fact that shear-induced turbulence is in most cases also present; it can be generated at the wall, such as in pipe flows, or due to large mean velocity gradients when the gas distribution is inhomogeneous, such as in unstable bubble columns. However, in a similar configuration as Lance & Bataille (1991), but with a more recent instrumentation, Larue de Tournemine (2001) obtained a spectrum evolving as k^{-3}. It seems therefore likely that bubble-induced turbulence generates a spectral range in k^{-n}, with an exponent n close to 3. Nevertheless, we still ignore at which wavelengths this range starts and stops. Generally speaking, we can say that a satisfactory description of the bubble-induced agitation required the knowledge of the characteristic scales of the various spectrum ranges.

The objective of the present work is to determine the main characteristics of the bubble-induced agitation at high Reynolds numbers and moderate volume fractions. To achieve this goal, we carried out an experimental study of a stable bubble column in which air bubbles of three different diameters ($d = 1.6$, 2.1 or 2.5 mm) are rising in water for moderate volume fractions ($0.005 \leqslant \alpha \leqslant 0.1$). The originality of this investigation is to consider both the steady flow within the homogeneous bubble swarm and the decaying agitation after the air injection has been stopped. First, the characteristic velocity scales of both the liquid and the bubbles are measured within the bubble swarm by means of dual optical probe and LDA. Second, the large scales of the spectrum of the liquid fluctuations are determined from particle image velocimetry
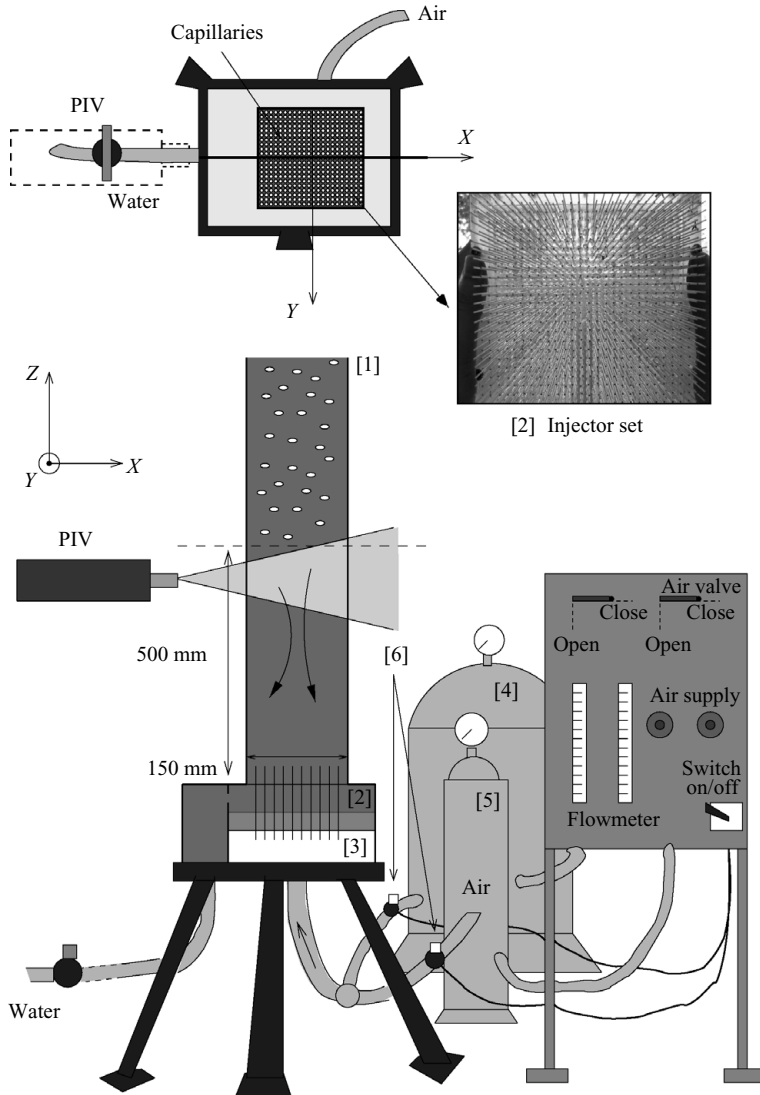
FIGURE 1. Experimental set-up.

(PIV) measurements in the region free of bubbles that immediately follows a swarm of rising bubbles. Then, the decay of the kinetic energy of the liquid agitation after the passage of the bubble swarm is used to determine the rate of dissipation.

The paper is organized as follows. The experimental set-up and the measurement techniques are detailed in §2. The results concerning the bubbles, the liquid agitation within and after the bubble swarm are successively presented in §§3, 4 and 5. Finally, the characteristic velocity and length scales as well as the dissipation rate are expressed as functions of the bubble diameter, the rise velocity of an isolated bubble and the gas volume fraction in §6.

2. Experimental set-up and instrumentation

The experimental set-up is depicted in figure 1. The test section [1] is an open tank of 1000 mm height with a squared cross-section of 150 mm width. To allow

d_c (mm)	N_c (−)	d (mm)	χ (−)	V_0 (mm s^{-1})	A (mm)	f (Hz)	θ (°)	Re (−)	We (−)	St (−)	Cd_0 (−)
0.10	841	1.6 ± 0.2	1.4	335	0	0	0	540	2.6	0	0.19
0.20	841	2.1 ± 0.1	1.7	320	4.9	4.6	25	670	3.1	0.030	0.27
0.33*	196	2.5	2.0	309	4.3	6.3	25	770	3.4	0.051	0.34
0.40	361	2.5 ± 0.2	2.0	305	5.2	5.0	28	760	3.3	0.041	0.35

TABLE 1. Characteristics of single rising bubbles for the three classes of capillaries: d_c, capillary inner diameter; N_c, number of capillaries in each injector set; $d = (6\vartheta/\pi)^{1/3}$, bubble equivalent diameter (ϑ is the bubble volume); χ, bubble aspect ratio; V_0, average vertical velocity; A, amplitude of the oscillatory path; f, path oscillation frequency; θ, maximal inclination of the bubble velocity; $Re = \rho\, d\, V_0/\mu$, Reynolds number (ρ and μ are the liquid density and viscosity); $We = \rho\, d\, V_0^2/\sigma$, Weber number ($\sigma$ is the interfacial tension); $St = f\, d/V_0$, Strouhal number; $Cd_0 = 4\, d\, g/(3\, V_0^2)$, drag coefficient; *, bubbles studied by Ellingsen & Risso (2001).

full optical access the four sides are of a glass construction. The tank is filled with filtered tap water and air bubbles are injected at the bottom through a removable set of injectors [2]. An injector set is constituted of a regular array of steel capillary tubes that open into a pressurized air chamber [3]. Capillaries of three different inner diameters, $d_c = 0.1$, 0.2 and 0.4 mm, are used to vary the bubble size (table 1). The system possesses three operating modes. First, isolated bubbles or bubble trains can be produced by using a single injector directly connected to pressurized air tank [4]. Second, a homogeneous swarm of rising bubbles is continuously generated when an injector set is inserted into the set-up and chamber [3] is connected to the pressure-controlled air tank [4]. The gas volume fraction α is controlled by adjusting the gas flow rate. The use of a large number of capillary tubes regularly distributed over the bottom cross-section of the tank ensures the generation of a stable bubble column (without large-scale recirculation flows) up to α of several tens of a percent. Then, it is possible to switch the connection of air chamber [3] from air tank [4] to air tank [5] by means of electrovalves [6]. The pressure in air tank [5] is low enough so that the bubble formation is suddenly stopped, but large enough so that no water can flow down through the capillary tubes to air chamber [3]. Since bubbles are no longer produced, we observe the rise of a bubble swarm followed by a region that is free of bubbles. This third operating mode allows us to study the wake developing behind a swarm of bubbles.

Below, we describe the experimental techniques used to investigate the two-phase flow. We shall not describe in detail high-speed imaging, dual optical probe and LDA, which are now classic techniques operated here similarly as in Ellingsen & Risso (2001) and Risso & Ellingsen (2002). In contrast, we shall detail the determination of the velocity spectra in the wake of the bubble swarm by PIV because it is an innovation of this work.

2.1. *Gas phase characterization*

First, a single capillary tube has been used to determine the size of the bubbles that are produced by each class of injectors and to characterize the bubble dynamics for the reference case of an isolated bubble ($\alpha \approx 0$). Vanishing volume fractions allows us to make use of accurate high-speed imaging techniques. Two perpendicular high-speed digital cameras were used to take pictures of the bubbles, the contours of which being then detected by image processing. It gives access to the bubble size, aspect ratio, velocity and orientation (table 1).

The equivalent bubble diameter has been measured just after the detachment from the tip of the capillary by both imaging and acoustic techniques. The acoustic technique (see Manasseh, Riboux & Risso 2008, for details) consists in measuring the frequency f_a of the sound emitted by the bubble, which is related to the bubble diameter by the expression

$$d = \frac{1}{\pi f_a} \sqrt{\frac{3\gamma P_0}{\rho}}, \qquad (2.1)$$

where P_0 is the water absolute pressure, γ the gas specific heat and ρ the liquid density. Measurements were carried out for different capillaries of each set and various gas flow rates, which corresponded to gas volume fractions ranging from 0 to 0.04 when the whole sets of injectors are used. Both methods lead to the same results. For small volume fractions, the bubble size is controlled by the static balance between buoyancy and surface tension and therefore does not depend on α. To the injectors diameters $d_c = 0.1$, 0.2 and 0.4 mm correspond the bubble diameters $d = 1.6 \pm 0.2$, 2.1 ± 0.1 and 2.5 ± 0.2 mm, respectively. The variations indicated after the symbol $\pm$ characterize the polydispersity due to discrepancies between the different capillary tubes of a given set. Up to $\alpha = 1.5\%$, the bubble sizes remain equal to the quasi-static value within the interval defined by the polydispersity. For larger α, we observed a regular increase of the bubble size with the gas volume fraction, which has been estimated by optical probe measurements within the bubble swarm: at $\alpha = 10\%$, the average diameter has been increased by 50 % for $d_c = 0.1$ mm, 40 % for $d_c = 0.2$ mm and 30 % for $d_c = 0.4$ mm.

Figure 2 shows examples of bubble evolutions along the trajectories and table 1 presents their main characteristics. As observed by Ellingsen & Risso (2001), the bubble takes a spheroidal shape with an aspect ratio χ between 1.4 and 2, their minor axis being parallel to their velocity. The smallest bubble ($d = 1.6$ mm) rises on a straight line whereas the others ($d = 2.1$ and 2.5 mm) follow an oscillatory path with an amplitude A close to 5 mm, a maximal inclination θ between 25° and 28° and an oscillation frequency f close to 5 Hz. The average vertical velocity ($V_0 = 309$–335 mm s^{-1}) is in agreement with the measurements performed by Maxworthy *et al.* (1996) for clean bubbles. It does not depend significantly on the bubble diameter for the considered bubbles; the Reynolds number ($540 \leqslant Re \leqslant 760$), the Weber number ($2.6 \leqslant We \leqslant 3.3$) and the drag coefficient ($0.19 \leqslant Cd_0 \leqslant 0.35$) thus vary essentially through the bubble size.

For $\alpha > 0$, the properties of the gas phase inside the bubble swarm are measured by means of optical probes. Each probe provides an electric signal, the magnitude of which depends on the optical index of the phase that surrounds the probe tip. This analogue signal is digitalized and recorded by a computer. A threshold is then applied to distinguish the gas from the liquid. A single optical microprobe with conical tip of 10 μm is used to determine the gas volume fraction. The sampling frequency has to be adjusted to ensure a correct bubble detection and the recording time has to be large enough to allow the statistical convergence. With a sampling frequency of 10 kHz and a recording times larger than 800 s, the gas volume fraction is obtained with an accuracy better than 2 %. Figure 3 presents various profiles of α at different locations within the test section and for different gas flow rates. Figure 3(*a*) shows that the bubbles are uniformly distributed in the central part of the tank (-40 mm $\leqslant X, Y \leqslant 40$ mm), whereas figure 3(*b*) shows that the gas volume fraction has reached a constant value for vertical elevations Z larger than 300 mm.
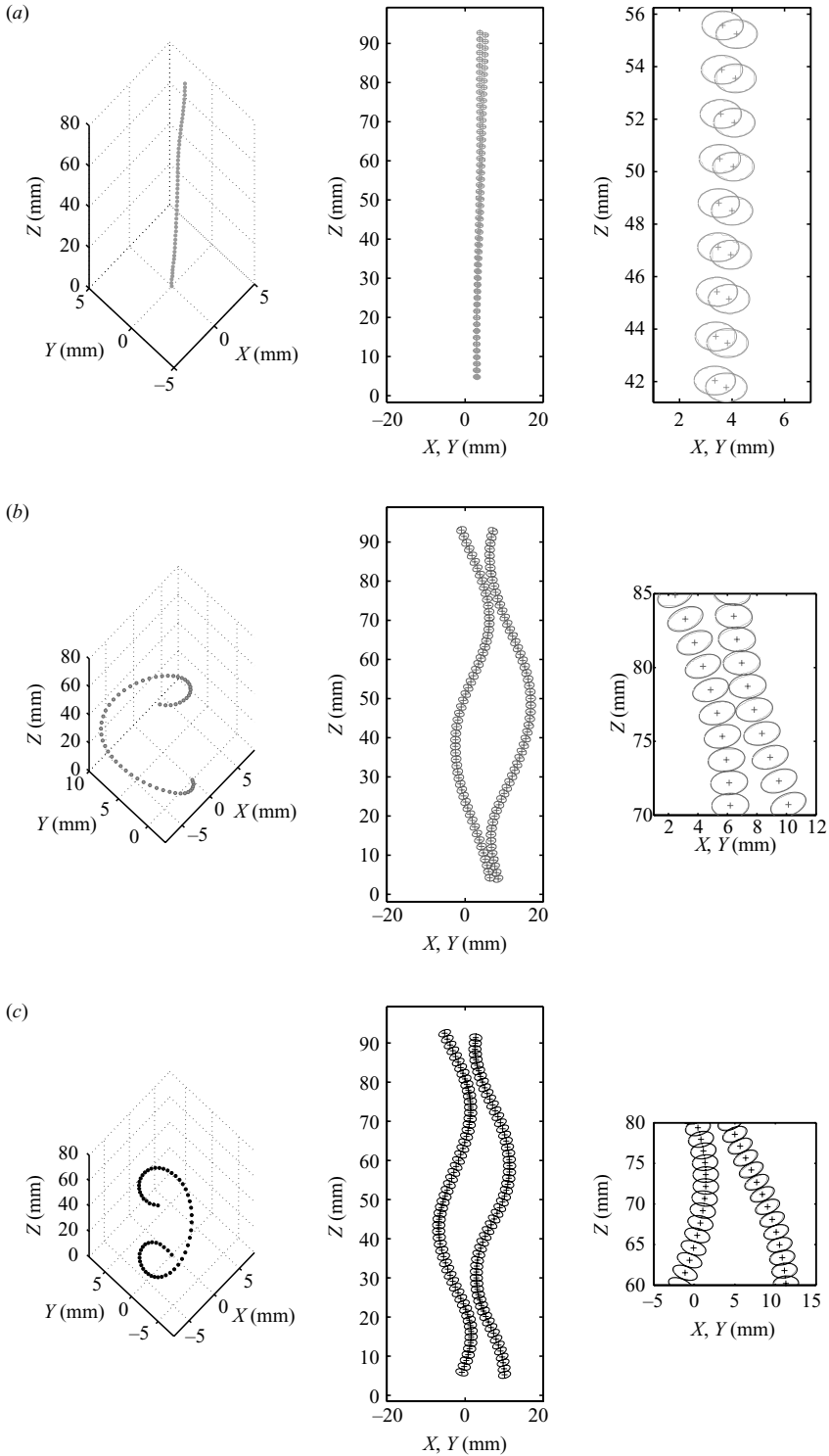
FIGURE 2. Bubble evolutions along the trajectories for the three different diameters: to the left, three-dimensional trajectories; in the middle, projection on the two camera planes; to the right, exact spheroids superimposed to experimental bubble contours: (*a*) $d = 1.6$ mm; (*b*) $d = 2.1$ mm; (*c*) $d = 2.5$ mm.
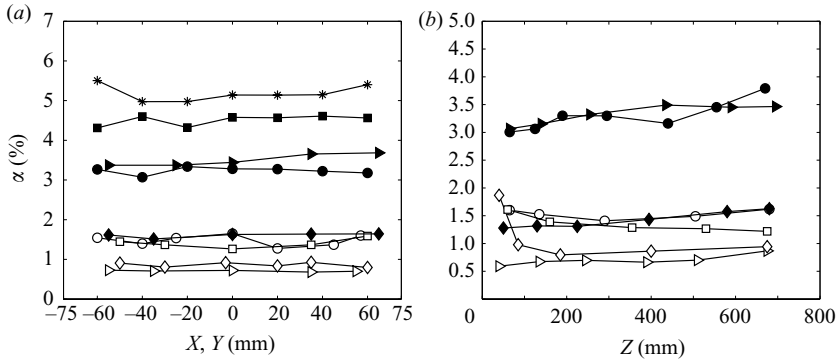
FIGURE 3. Gas volume fraction α at different locations for $d_{eq} = 2.5$ mm: (*a*) horizontal profiles along X or Y at $Z = 500$ mm; (*b*) vertical profiles at the centreline of the tank ($X = Y = 0$ mm). Different symbols correspond to different gas flow rates.

In the following, all presented results have been obtained at a single point located in the middle of the tank ($X = Y = 0$), where the swarm is uniform, and at $Z = 500$ mm, where the regular distribution of the capillaries has been forgotten.

A dual optical probe is used to measure bubble velocities. The two probes are separated by a vertical distance $d_p = 0.54$ mm. The signal provided by each probe is first processed as that of the single probe. Since the distance between the probe is at least three times smaller than the bubble diameter, it is possible to associate unambiguously the successive passages of a bubble on the two probes and to determine the corresponding time interval Δt. For each detected pair of bubble, the ratio $d_p/\Delta t$ provides a sample of bubble vertical velocity V. Due to interactions with the first probe, some bubbles are detected by the first probe but not by the second. In other rare cases, two different bubbles touch quasi simultaneously the two probes, leading to unrealistic large velocities. These erroneous cases are discarded by applying an upper and a lower thresholds on Δt. Finally, PDFs of the bubble velocity are thus obtained (see figure 9). This method has been validated by Kiambi *et al.* (2003) who compared its results with those obtained by mean of high-speed imaging. It allows an accurate determination of the bubble average vertical velocity $\langle V \rangle$. On the other hand, it overestimates the fluctuations of the bubble velocity because it also accounts for fluctuations of the bubble orientation. The variance obtained from this method is however a good parameter to characterize the overall bubble agitation and is used for that purpose in §3. Also, it is worth mentioning that for the bubble volume fraction, residence time and size considered, coalescence was not observed.

2.2. *Measurements of liquid fluctuations within the bubble swarm*

The liquid velocity inside the bubble swarm has been measured by means of a two-component LDA operated in forward-scattering mode. The LDA system consists of an Ar-ion laser source (Spectra Physics 2016) with a DANTEC optical arrangement that includes two photo-multipliers equipped with green and blue filters, and two burst spectrum analysers (DANTEC 57N10). The LDA provides measurements of the vertical component of the liquid velocity (Z direction) and one horizontal component (Y direction). The two measurement volumes are ellipsoids with a major axis of 0.15 mm in the X direction, and two minor axes of 0.04 mm in the Y and Z directions. Due to the interception of the laser beams by the bubbles, the LDA data rate decreases with the gas volume fraction. A few decigrams of Iriodin 111 was thus
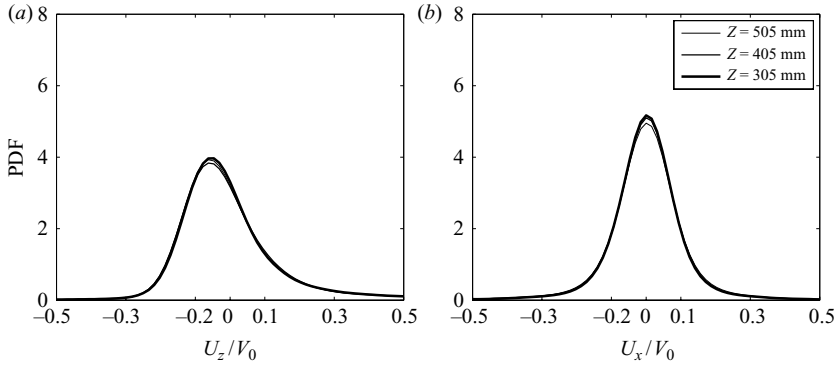
FIGURE 4. PDF of liquid velocity fluctuations at various elevations Z for $d = 2.1$ mm and $\alpha = 0.007$: (*a*) vertical component U_z/V_0; (*b*) horizontal component U_x/V_0.

added to the water and allowed us to obtain data rates of 80 Hz at $\alpha = 0.005$ and 10 Hz at $\alpha = 0.04$. Recording durations ranging from 8×10^2 s and 1.2×10^3 s were used to ensure a number of samples of at least 10^4 for all investigated cases. The optical and electronic adjustments of the LDA set-up are the same as those used by Ellingsen & Risso (2001) who showed that the PDFs of horizontal and vertical liquid velocities, U_x and U_z, were obtained without bias in the range $-0.7\langle V \rangle - 0.7\langle V \rangle$. Figure 4 shows PDFs of U_x and U_z measured at three different elevations in the tank, $Z = 305$, 405 and 505 mm. The three curves are similar, confirming that the bubble swarm has reached a state independent of the elevation for $Z \geqslant 300$ mm.

2.3. *Measurements of liquid-fluctuation moments and spectra in the swarm wake*

A major objective of the present investigation was to determine the length scales of the liquid agitation. This cannot be obtained by LDA since it requires simultaneous measurements of the liquid velocity in various locations. Also, whatever the experimental technique, this can hardly be achieved inside the bubble swarm where the bubbles cause any measured signal to be discontinuous. To overcome these difficulties, we decided to measure the velocity field after the passage of the bubble swarm by means of a fluorescent high-speed PIV technique. This has two drawbacks: (i) since the measuring window is fixed, we are considering an unsteady flow that evolves as the bubbles rise away; (ii) we need to determine whether the properties of the swarm wake are significant of the flow within the homogeneous swarm. These points, which concern the physical interpretation, will be addressed later in the sections devoted to the presentation of the results. Here, we focus on the description and the validation of the experimental method.

Small particles of encapsulated rhodamine (≈ 10 μm, 1.5 g cm^{-3}) are added to the water to serve as fluorescent tracers; they can be considered as neutrally buoyant as they take several hours to sediment through the whole test section. No modification of the swarm dynamics was observed due to the presence of these tracers. A 10 mJ Yag laser (New wave, Pegasus) generates a vertical sheet of light of wavelength 527 nm with a thickness of about 0.8 mm. A high-speed video camera (Photron ultima APX) synchronized with the laser pulses acquires digital images of 1024×1024 pixels. The measurement window is a square of 5.12 cm width located 400 mm above the injectors in vertical mid-plane of the tank. The resulting pixel size is thus 0.05 mm. The laser light is maximum within the measurement window where its variation is less than 3 %. The PIV acquisition is started after the stationary bubble swarm has developed while the air injection is still running. Then, the injection is stopped and
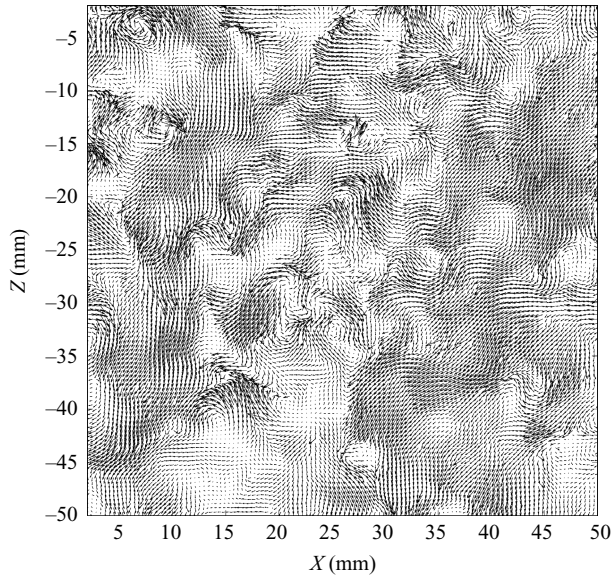
FIGURE 5. Instantaneous liquid velocity field measured by PIV behind the bubble swarm using interrogation cells of 16×16 pixels ($d = 2.5\,\mathrm{mm}$, $\alpha = 0.0046$).

the PIV recording is continued. Since the bubbles inside the swarm are rising more slowly than an isolated bubble, the interface between the bubbly region – where the gas volume fraction is uniform – and the single-phase region – which follows the swarm – remains sharp. It is flat in the middle of the tank and curved downward close to the wall where the bubbles rise more slowly. In the following, the time origin is defined as the instant corresponding to the first image where no bubble is present.

The frame rate is fixed at 200 Hz and the velocity field is calculated between each pair of consecutive images by means of the PIV code developed in our laboratory (Cid & Gardelle 2005). Classic iterative algorithms using subpixel image shift and deformation are used. The PIV parameters are adjusted to optimize the computation of the velocity field in the absence of the bubbles for interrogation cells of 8×8 or 16×16 pixels: the measured displacements range between $1/10$ and $1/4$ of the width δ of the interrogation cells, which each contains at least 10 particles. Velocity vectors are computed every $\delta/2$ by overlapping interrogation cells of 50 %. Then, vectors located at less than $n\delta$ from the borders are removed to avoid border errors in the computational algorithm: $n = 8$ for the 8×8 case and $n = 6$ for the 16×16 case. Figure 5 shows an example of raw velocity field computed with interrogation cells of 16×16 pixels. It is worth noting that this field is the direct result of the PIV computation without any suppression of erroneous vectors. The reproducibility and the statistical convergence have been checked by performing each experiment three times.

The energy of the fluctuations is slightly higher at the top of the measurement window, which is closer to the rear of the bubble swarm. However, calculating the standard deviation of the liquid velocity over the whole measurement window without taking into account the inhomogeneity in the vertical direction leads to an error of only 2.5 %. Consequently, we shall assume that the fluctuations are homogeneous over the measurement windows and use all the corresponding velocity vectors to estimate statistical quantities. In particular, the spatial spectrum of the vertical velocity S_{zz} is calculated by means of a fast Fourier transform (FFT) for each vertical column
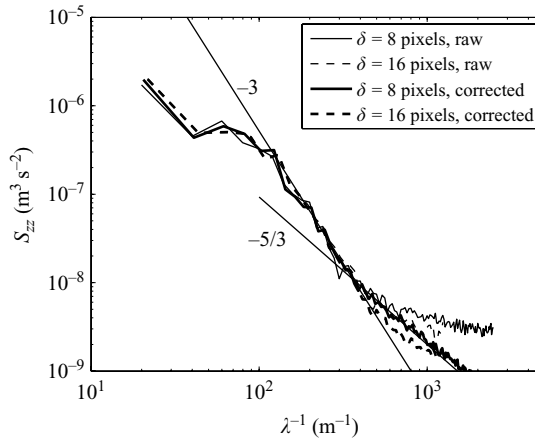
FIGURE 6. Spectra of vertical fluctuations computed from PIV velocity fields obtained by using either interrogations cells of 8×8 or 16×16 pixels. The spectra computed from raw data are compared with those computed from data that are interpolated after suppression of false vectors ($d = 2.5$ mm, $\alpha = 0.0046$).

of the two-dimensional PIV velocity field and then averaged over all the columns. The average spatial spectrum of the horizontal velocity S_{xx} is obtained in the same manner from the horizontal rows of the PIV velocity field.

Figure 6 shows PIV spectra of the vertical velocity obtained for $\alpha = 0.005$ and $d = 2.5$ mm. Hereinafter, all the spectra will be plotted as a function of the reciprocal of the wavelength (λ^{-1}) instead of the wavenumber ($k = 2\pi\lambda^{-1}$) because it is more convenient to make comparisons with characteristic length scales, as the bubble diameter. Note that the energy of wavelengths λ smaller than the cell size δ is filtered out. The Nyquist–Shannon sampling theorem states that the smallest resolved wavelength is twice the signal sampling step. Since the velocity vectors are computed every $\delta/2$, the smallest wavelength resolved in the spectra is therefore δ and corresponds to the filtering scale of the PIV meshgrid. The spectra computed with cells of 16×16 pixels (dashed lines) are thus defined for λ larger than $\delta = 0.8$ mm, whereas those computed with cells of 8×8 pixels (solid lines) are defined for λ larger than $\delta = 0.4$ mm. The spectra computed from the 16×16 and 8×8 raw PIV velocity fields (thin lines) are identical for λ larger than 1.5 mm and slightly differ for smaller ones. This indicates the existence of a PIV noise at small scales due to some erroneous PIV velocity vectors.

Westerweel & Scarano (2005) developed a general method to detect such spurious vectors. This method is based on a normalized median test applied to the PIV displacement vector field Δ. For each point i, the residual is defined as the absolute value of the difference between Δ_i and the median value Δ_{im} of the eight surrounding points: $r_i = |\Delta_i - \Delta_{im}|$. Then, the median value of the residual r_{im} is calculated over the eight surrounding points. Finally, the normalized residual is defined by

$$r_i' = \frac{r_i}{r_{im} + \varepsilon}, \tag{2.2}$$

where ε is a parameter that fixes the acceptable level of fluctuation of the residual test. A measurement is considered erroneous when the corresponding normalized residual r_i' is larger than a given threshold r_{max}'. The optimal values, $\varepsilon = 0.1$ pixel and $r_{max}' = 2$, have been determined from numerous tests involving flows of various Reynolds numbers ranging from 10^{-1} to 10^7. Applied to the present PIV results, this method detects 3.6 % false vectors for the computation using 16×16 cells and 16 %
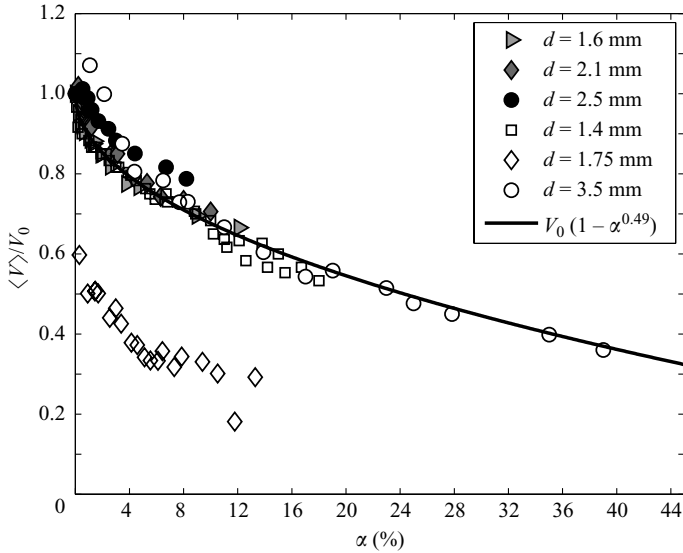
FIGURE 7. Average bubble velocity $\langle V \rangle$ normalized by the velocity V_0 of a single rising bubble as a function of the gas volume fraction α: filled symbols, present work; $\square$, Zenit *et al.* (2001); $\diamond$, Larue de Tournemine (2001); $\bigcirc$, Garnier *et al.* (2002).

for those using 8×8 cells. After suppression of the false vectors, a regularly sampled two-dimensional velocity field is reconstructed by using the *griddata* Matlab function, which is based on Delaunay's triangulation. The thick lines in figure 6 represent the corrected spectra calculated after suppressions of false vectors and interpolations. First of all, we remark that the four spectra match for λ larger than 2 mm. The region of the spectra that exhibits a λ^3 power law is thus observed for both cell sizes and whatever spurious vectors are suppressed or not. There is therefore no doubt about the existence of this particular power law behaviour in this range of λ. Then, we observe that the best-resolved raw and corrected spectra (solid lines) match for λ larger than about 1.4 mm, indicating that the $\lambda^{5/3}$ law, which is observed to follow the λ^3 law, is not an artifact due to PIV noise. Actually, the best-resolved corrected spectra (thick solid line) follows the $\lambda^{5/3}$ trend while λ is larger than 0.6 mm, and it is only for smaller wavelengths that a plateau due to the sampling noise is reached. We are therefore confident that the spectra computed from 8×8 PIV results are correct for all wavelengths larger than 0.6 mm. In the following, we shall only present the best-resolved corrected spectra up to this limit.

3. Dynamics of the bubbles

We start with the description of the gravity-driven motion of the bubbles, which is the cause of the flow. Figure 7 shows the average bubble velocity $\langle V \rangle$ as a function of the gas volume fraction for $0.002 \leqslant \alpha \leqslant 0.12$ and the three different bubble diameters. The velocity is normalized by the average velocity V_0 of a single rising bubble, which corresponds to a vanishing volume fraction. Note that the three values of V_0 differ by less than 10 % (see table 1) because the investigated diameters belongs to the region where the rise velocity against the bubble diameter reaches a maximum (see figure 5 in Maxworthy *et al.* 1996). Figure 7 also presents results of previous experimental studies. Zenit *et al.* (2001) and Martinez-Mercado *et al.* (2007) investigated a stable bubble column quite similar to ours; for sake of clarity only the results of Zenit *et al.* (2001) are plotted in the present figure. For air–water bubbles of 1.4 mm diameter,
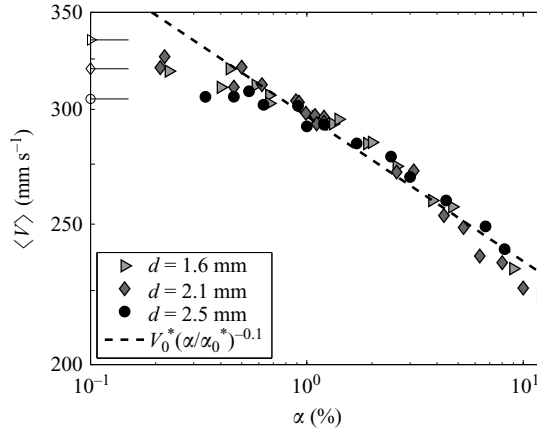
FIGURE 8. Average bubble velocity $\langle V \rangle$ against the gas volume fraction α. Dashed line: (3.1) with $V_0^* = 0.318$, $\alpha_0^* = 0.005$. Open symbols at $\alpha = 0$ correspond to single rising bubbles.

their results are in good agreement with ours. The investigations of Roig & Larue de Tournemine (2007) and Garnier *et al.* (2002) also considered homogeneous bubbly flow, but with a non-zero liquid upward velocity $\langle U \rangle$; consequently $\langle V \rangle$ is then defined as the mean bubble velocity minus the mean liquid velocity. Garnier *et al.* (2002) investigated a pipe flow with $\langle U \rangle$ less than $0.06\,\mathrm{m\,s^{-1}}$ and their results for $d = 3.5\,\mathrm{mm}$ are close to those obtained in stable bubble columns provided the gas volume fraction is larger than 4 %. Roig & Larue de Tournemine (2007) investigated a channel flow with a larger mean liquid velocity, between 0.45 and $0.59\,\mathrm{m\,s^{-1}}$; for $d = 1.75\,\mathrm{mm}$, they found that $\langle V \rangle$ is much smaller than the rise velocity of a single bubble in a fluid at rest and that its evolution with α is different. This is probably due to the fact that the bubbles are observed to be more deformed in their experiment because of the shear-induced turbulence generated by the channel flow. In every case, the hindrance effect makes $\langle V \rangle$ to be a decreasing function of α. Provided the effect of the mean liquid velocity and the corresponding shear-induced turbulence are negligible, this function is reasonably approximated by $\langle V \rangle = V_0\,(1 - \alpha^{0.49})$.

Martinez-Mercado *et al.* (2007) reported a discontinuity between V_0 and the measured values of $\langle V \rangle$ for α of a few tenths of a percent. The same trend is observed in figure 7. One may thus wonder whether the rise velocity of the isolated bubble is the relevant velocity scale for $\langle V \rangle$ in the range of volume fraction investigated here. To clarify this point, the present results are plotted in dimensional form in figure 8. Rather than a discontinuity, we observe a continuous transition, which depends on d, between V_0 and the value of $\langle V \rangle$ at $\alpha_0^* = 0.005$. Then for $\alpha \geqslant \alpha_0^*$, the values of $\langle V \rangle$ collapse on a master curve for $\alpha_0^* \leqslant \alpha \leqslant 0.1$, which is approximated well by

$$\langle V \rangle = V_0^*\,(\alpha/\alpha_0^*)^{-0.1} \quad \text{with} \quad V_0^* = 0.318\,\mathrm{mm\,s^{-1}}. \tag{3.1}$$

Now we consider the agitation of the bubbles. Figure 9 shows the PDFs of the bubble velocity fluctuations for the three diameters and various volume fractions. All PDFs have the same asymmetric shape, strong upward fluctuations being more probable than strong downward ones. For a given bubble diameter, the PDFs do not evolve visibly with the gas volume fraction. This independence of the bubble velocity fluctuations upon α was already noticed for a narrow range of volume fractions ($0.005 \leqslant \alpha \leqslant 0.01$) and a single bubble diameter ($d = 2.5\,\mathrm{mm}$) by Risso & Ellingsen (2002) and then reported by Martinez-Mercado *et al.* (2007) for broad ranges of Reynolds numbers ($50 \leqslant Re \leqslant 500$) and volume fractions ($0.01 \leqslant \alpha \leqslant 0.1$).
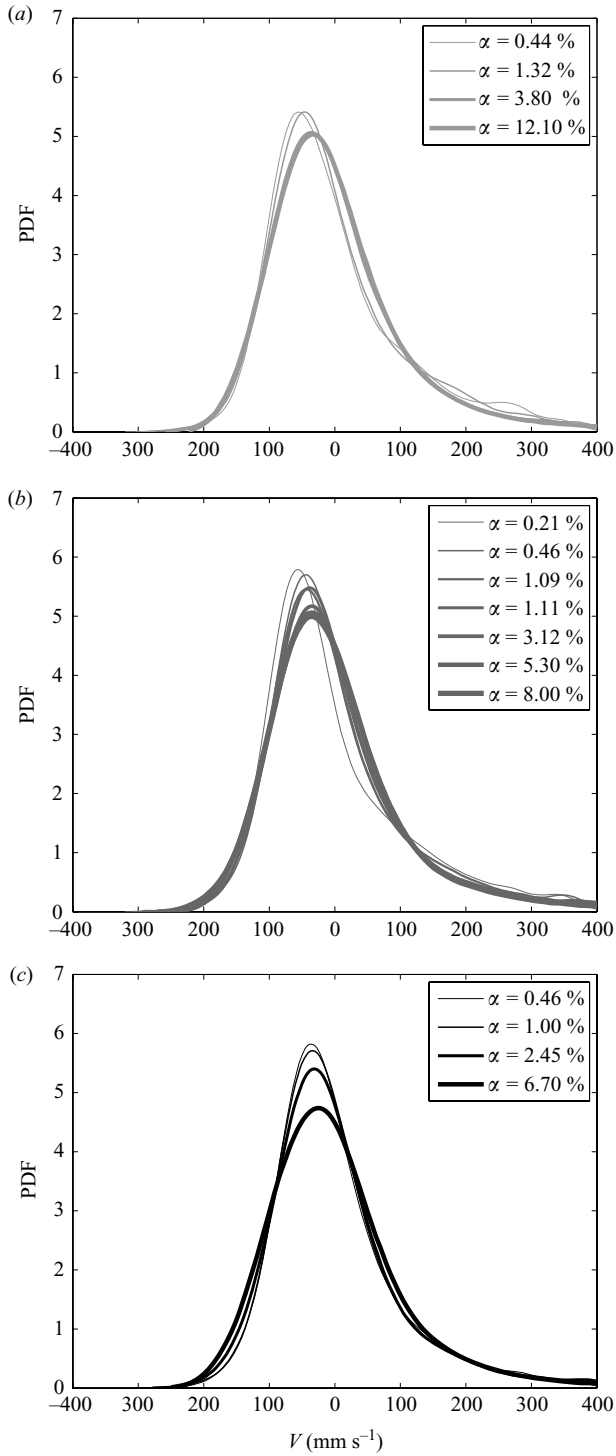
FIGURE 9. Centred PDFs of the bubble velocity V as a function of the gas volume fraction α: (*a*) $d = 1.6$ mm; (*b*) $d = 2.1$ mm; (*c*) $d = 2.5$ mm.
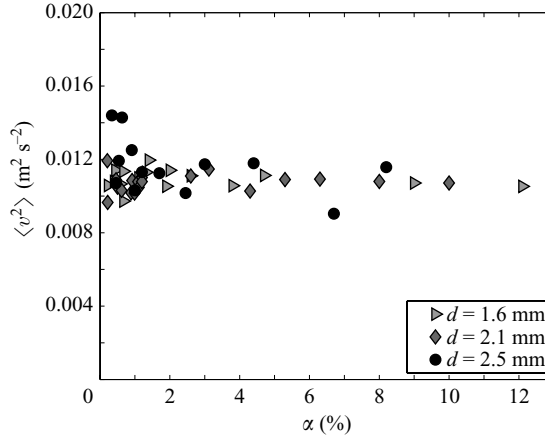
FIGURE 10. Variance $\langle v^2 \rangle$ of the bubble velocity against the gas volume fraction α for the three bubble diameters.

Provided the Reynolds number is large enough, the wake of a single bubble becomes unstable and the bubble performs path oscillations. This explains why the agitation of the bubbles may not vanish as α tends towards zero. Then, when α increases the bubble agitation does not evolve as long as the contribution of the path oscillations dominates over bubble interactions. This interpretation seems to not hold for the smallest bubbles considered here ($d = 1.6\,\mathrm{mm}$) since an isolated bubble of the same size has a stable wake and rises at constant velocity on a straight path. However, we observe path oscillations at finite gas volume fraction as small as 0.2 %. Slight perturbations due to hydrodynamic interactions between the bubbles are thus capable to initiate path instabilities. But once the path oscillations have started, their amplitudes are independent of the magnitude of these perturbations.

Figure 10 confirms that the bubble velocity variance is constant from α_0^*. Moreover, this constant ($\approx 11 \times 10^{-2}\,\mathrm{m^2\,s^{-2}}$) is the same for the three investigated diameters. Therefore, even if the velocities of the single rising bubbles differ slightly between the three diameters investigated, the bubble average velocity as well as the bubble fluctuations are the same for the three diameters in the range $0.005 \leqslant \alpha \leqslant 0.1$. This leads to two important conclusions. First, we would like to stress that even if this paper deals with moderate volume fractions, the regime that is investigated do not correspond to the limit of very dilute volume fractions where bubble interactions are totally negligible. Second, since the velocity scale is the same for all three considered diameters, all disparities between the results corresponding to the different bubble sizes will only result from the change of length scale. In other words, the Reynolds or the Weber numbers will only differ due the diameter change.

4. Dynamics of the liquid within the bubble swarm

Figure 11 shows the normalized PDFs of the two components of the liquid fluctuations for various volume fractions and the three bubble diameters. Vertical fluctuations (first column) are not isotropic, large upward fluctuations being more probable due to the entrainment of the flow in the wake of the bubbles. On the other hand, horizontal PDFs are symmetric since the flow generated around each bubble is axisymmetric in average and the horizontal bubble distribution is statistically uniform. A semi-log plot of the same data is presented in figure 12 to make visible that the
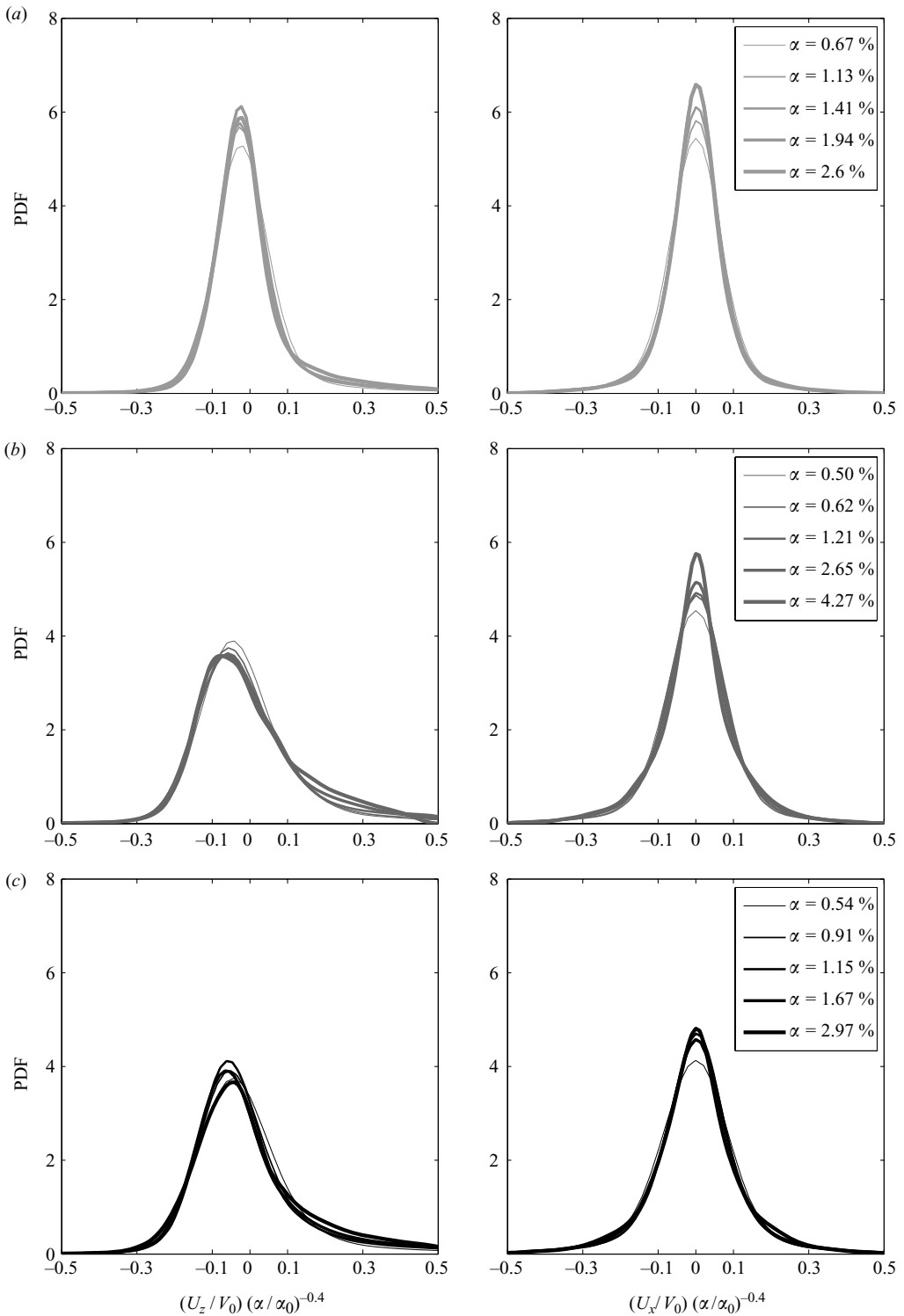
FIGURE 11. Normalized PDFs of vertical and horizontal liquid velocity fluctuations: (*a*) $d = 1.6$ mm; (*b*) $d = 2.1$ mm; (*c*) $d = 2.5$ mm ($\alpha_0 = 0.01$ and V_0 is the velocity of a single rising bubble).
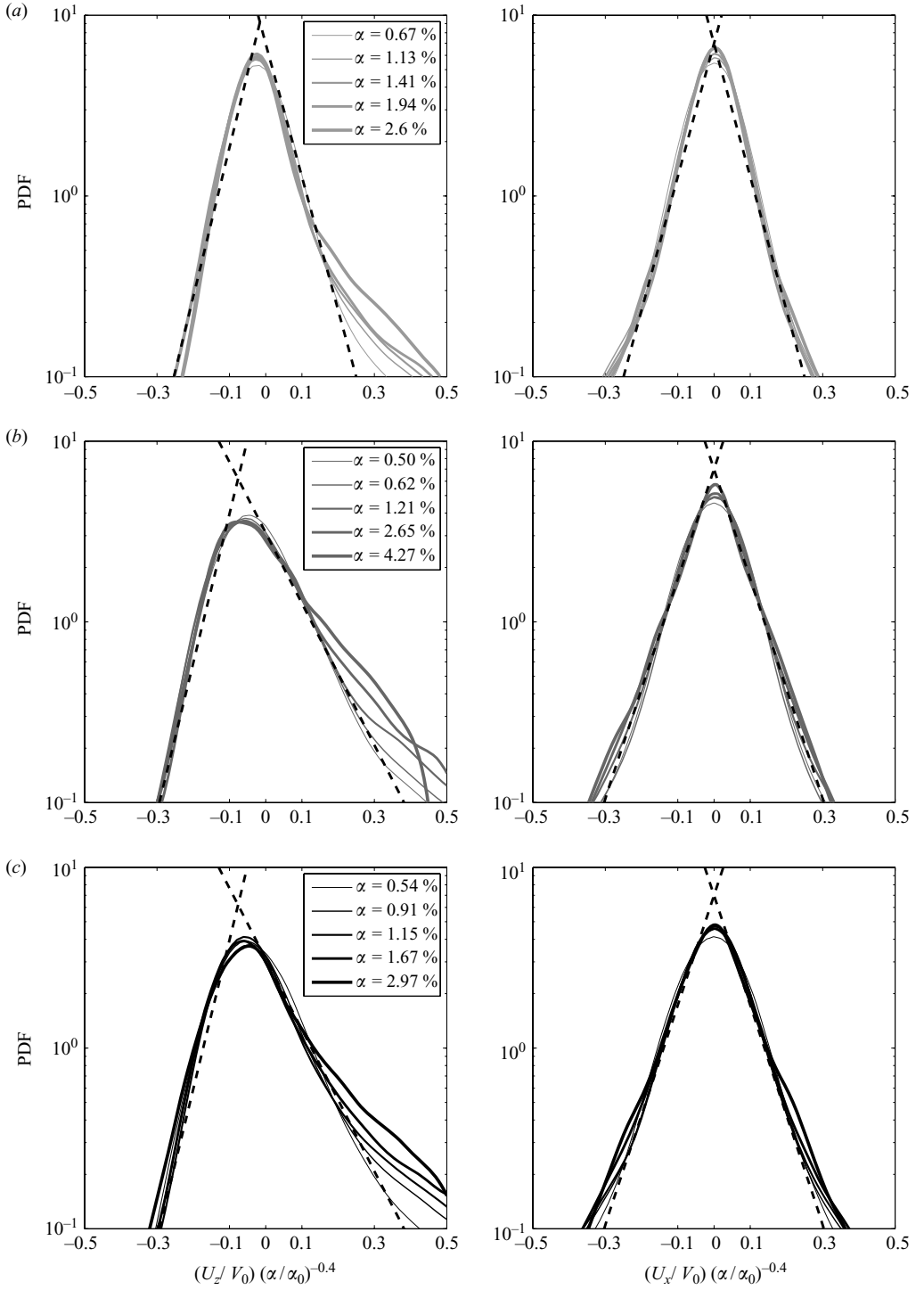
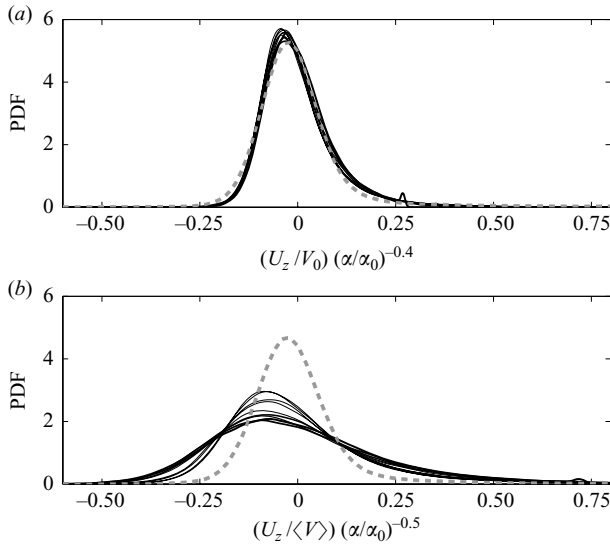FIGURE 12. Semi-log plots of the PDFs shown in figure 11.

FIGURE 13. Normalized PDF of vertical liquid velocity fluctuations: solid lines, data of Larue de Tournemine (2001) for $d = 1.75$ mm and various gas volume fractions in the range $0.015 \leqslant \alpha \leqslant 0.14$; dash line, present results for $d = 1.6$ mm. Normalization by either $V_0 \alpha^{0.4}$ (*a*) or $\langle V \rangle \alpha^{0.5}$ (*b*).

probability decays exponentially as the fluctuations increase. Note that if the velocity fluctuations were the sum of the velocity perturbations induced by an infinite number of bubbles, the central-limit theorem should imply to observe a Laplace–Gauss probability function. However, the number of bubbles in any finite volume surrounding the measurement point is finite because so is the gas volume fraction. That is the reason why we can observe asymmetric PDFs in the vertical direction as well as exponential decays, which are slower than the Gaussian decay but fast enough to ensure that all statistical moments are finite. It is interesting to note that such an exponential decay has been observed by Abbas & Climent (2006) for suspensions in the Stokes regime at volume fractions of a few percents. The fact of finding an exponential decay for radically different hydrodynamics confirms that this behaviour is rather related to statistical convergence than to the nature of the flow induced by the bubble motion.

Figures 11 and 12 also show that the PDFs are self-similar when varying the gas volume fraction provided the velocity fluctuations are normalized by

$$u = V_0 \alpha^{0.4}. \tag{4.1}$$

This scaling was first found by Risso & Ellingsen (2002) for a single bubble size ($d = 2.5$ mm) and a narrow range of gas volume fractions ($0.005 \leqslant \alpha \leqslant 0.01$). It was then confirmed for a broad range of Reynolds number by Martinez-Mercado *et al.* (2007) who used mixtures of water and glycerin of various concentrations. It is here confirmed again for bubbles rising in water for three different diameters and volume fractions up to 0.05. To check the validity of this self-similarity at larger gas volume fractions, we also determined the PDFs of the vertical fluctuations from the data of Larue de Tournemine (2001), which correspond to $d = 1.75$ mm and volume fractions ranging from 0.015 to 0.14. Figure 13 (upper part) shows that the normalized PDFs match very well our results for bubbles of 1.6 mm. The scaling $V_0 \alpha^n$ is thus proved to be valid up to $\alpha = 0.14$ with an exponent $n = 0.4 \pm 0.02$.
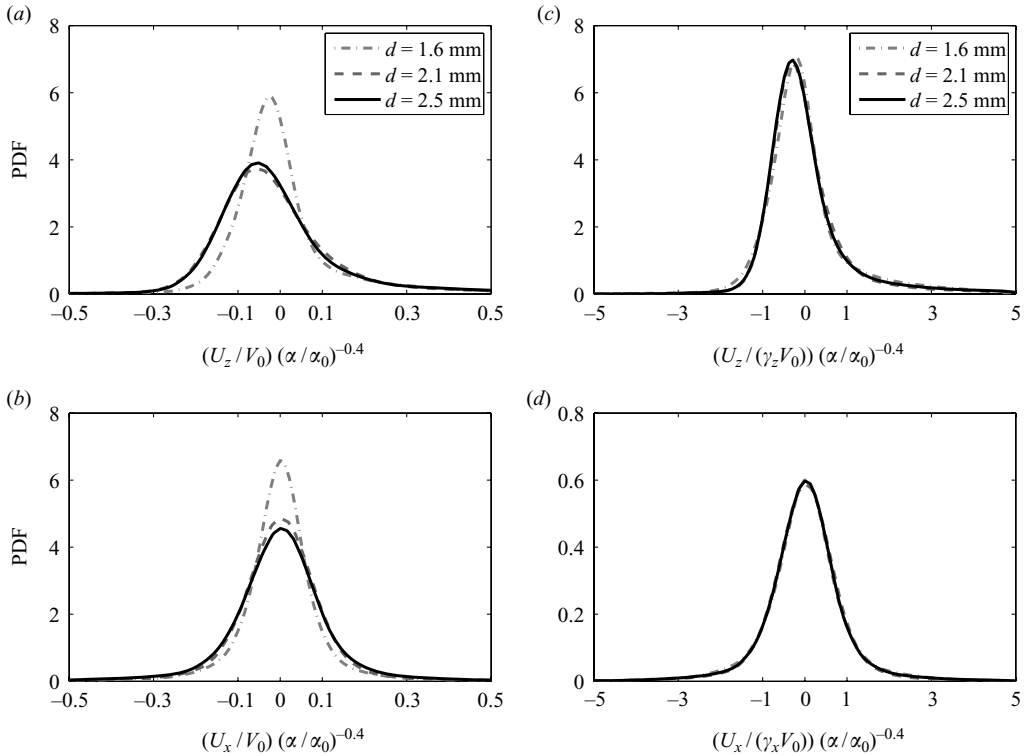
FIGURE 14. Self-similar PDFs of the liquid velocity fluctuations normalized by either $V_0 \alpha^{0.4}$ or $\gamma_i V_0 \alpha^{0.4}$, where γ_i is the standard deviation of the normalized velocity fluctuations: $\gamma_x = 0.09$ and $\gamma_z = 0.12$ for $d = 1.6$ mm; $\gamma_x = 0.12$ and $\gamma_z = 0.18$ for $d = 2.1$ mm; $\gamma_x = 0.13$ and $\gamma_z = 0.18$ for $d = 2.5$ mm.

It is worth recalling that the velocity V_0 used in (4.1) corresponds to the rise velocity of a single bubble. In the range of parameters considered in the present work, the average velocity $\langle V \rangle$ of the bubbles inside the swarm has been found to be proportional to $\alpha^{-0.1}$ (defined in (3.1)). From the present results, it is thus equivalent to consider that the velocity fluctuations scale as $u = V_0 \alpha^{0.4}$ or $u = \langle V \rangle \alpha^{0.5}$. From a practical point of view, it is more relevant to normalize the present PDFs by using V_0 as velocity scale since the small experimental uncertainty in the determination of $\langle V \rangle(\alpha)$ would slightly increase the scattering of the PDFs. Moreover, in the case investigated by Roig & Larue de Tournemine (2007), the evolution of $\langle V \rangle$ with α is totally different (figure 7) and therefore allows us to distinguish the two relations: the scaling $V_0 \alpha^{0.4}$ make the PDFs obtained for various volume fractions to collapse (figure 13a) whereas the scaling $\langle V \rangle \alpha^{0.5}$ (figure 13b) does not. This seems thus to confirm that the velocity fluctuations scale as $\alpha^{0.4}$ times a velocity scale that does not depend on α. One can doubt that this velocity is actually the average velocity of a single rising bubble, the physical relevance of which is difficult to interpret for $\alpha > 0$. It could rather be the velocity scale $(gd)^{1/2}$ related to the buoyancy force, which balances the drag force on each bubble. Nevertheless, PDFs obtained for more contrasted bubble diameters are required before to conclude about this point.

Figure 14(a, b) compare the normalized self-similar PDFs of the horizontal and vertical fluctuations obtained for the three different bubble diameters. The results for the two larger diameters ($d = 2.1$ and 2.5 mm) are similar while the PDFs

corresponding to the smallest diameter ($d = 1.6$ mm) are slightly narrower. We determined the standard deviation $\gamma_i(d)$ of each normalized PDFs: $\gamma_x = 0.09$, $\gamma_z = 0.12$ for $d = 1.6$ mm; $\gamma_x = 0.12$, $\gamma_z = 0.18$ for $d = 2.1$ mm; $\gamma_x = 0.13$, $\gamma_z = 0.18$ for $d = 2.5$ mm. Figure 14(c, d) show that after normalization by their standard deviation, the PDFs for the smallest diameter now collapse with the two others. The only difference is therefore that liquid fluctuations for the smallest bubbles have slightly less energy. The ratio of the vertical to horizontal standard deviations, which characterizes the anisotropy of the liquid fluctuations, is close to 1.4 for the three investigated diameters.

5. Liquid velocity fluctuations behind the bubble swarm

We investigate now the flow that develops behind the bubble swarm after the gas injection has been stopped. Figure 15 shows the time evolution of the standard deviations, u_z and u_x, of the velocity fluctuations measured by PIV in a fixed window located in the middle of the tank (see §2.3), for the three diameters and various volume fractions. The record was started before air injection was stopped. The first PIV measurements are thus noisy due to the presence of bubbles in the measurement section. It is however clearly visible that the energy of the fluctuations inside the bubble swarm is constant. For larger times, the magnitude of the fluctuations then decays as the bubble swarm rises up away from the measurement section. We first defined the origin of the time t as the instant t_0 when the last bubble leaves the measurement window. But since the last bubble visible in the PIV images is located close to the wall, its rise velocity is lower than the rise velocity of the swarm rear in the middle of the channel. The decay of the fluctuations starts therefore before t_0. In order to reveal a power-law decay by the use of a logarithmic representation, the time abscissa in figure 15 has been shifted by introducing a virtual origin t_v: $t^* = t - t_v$, In all considered cases and for both components, the fluctuating velocity decays as t^{*-1} during the first regime that occurs behind the bubble swarm. Provided they are normalized by their value at a given instant, say $t_0^* = t_0 - t_v$, the standard deviations write

$$\frac{u_i}{u_{i0}} = \frac{t_0^*}{t^*}. \tag{5.1}$$

Note that the value of the virtual origin t_v has been adjusted to obtain the best fit by expression (5.1): $t_v = -0.4$ s for $d = 1.6$ and 2.5 mm, $t_v = -0.5$ s for $d = 2.1$ mm. This regime of decay lasts approximately 0.4 s, which is the time for the bubbles to travel about 15 cm.

The solid lines in figure 16 represent the PDFs of the horizontal and vertical velocity fluctuations normalized by their standard deviation, for the largest bubble size ($d = 2.5$ mm). The results are plotted in semi-log for various instants belonging to the first regime of decay ($0.01 \leqslant t \leqslant 0.3$ s) and three different volume fractions ($\alpha = 0.0046$, 0.025 and 0.07). Whatever the volume fraction, the normalized PDFs do not depend on time. This self-preserving behaviour indicates that the decay of the fluctuating energy does not affect the statistical distribution of the fluctuations. The dashed lines represent the inner PDFs measured inside the bubble swarm ($t < 0$) which differ from the downward PDFs obtained for $t > 0$. While the fluctuations inside the bubble swarm come from perturbations generated at any distance from the bubbles, the fluctuations observed behind the bubble swarm only result from bubble wake interactions. Thus, the differences between the inner and the downward PDFs give us an idea of the relative contributions of the individual perturbations generated in the vicinity of each bubble and the collective fluctuations produced by wake interactions.
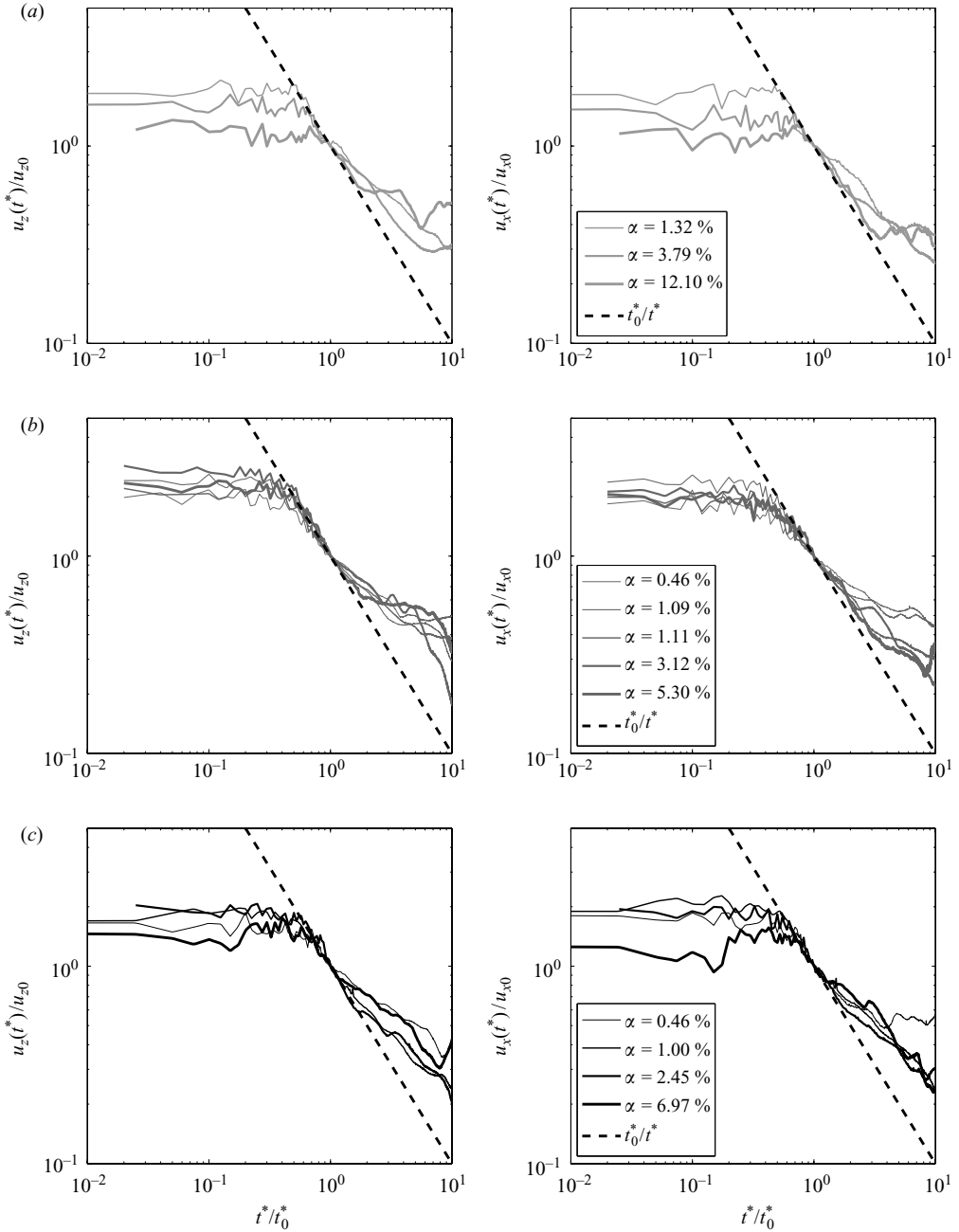
FIGURE 15. Time evolutions of the standard deviations of the liquid velocity fluctuations after the passage of the bubbles normalized by their values at time t_0: (*a*) $d = 1.6$ mm; (*b*) $d = 2.1$ mm; (*c*) $d = 2.5$ mm.

While PDFs measured inside the bubble swarm are clearly non-Gaussian, PDFs measured behind it become Gaussian: horizontal PDFs are approximately parabolic and vertical ones come to be symmetric as the volume fraction increases. The large fluctuations responsible for the non-Gaussian behaviour are thus mostly generated in
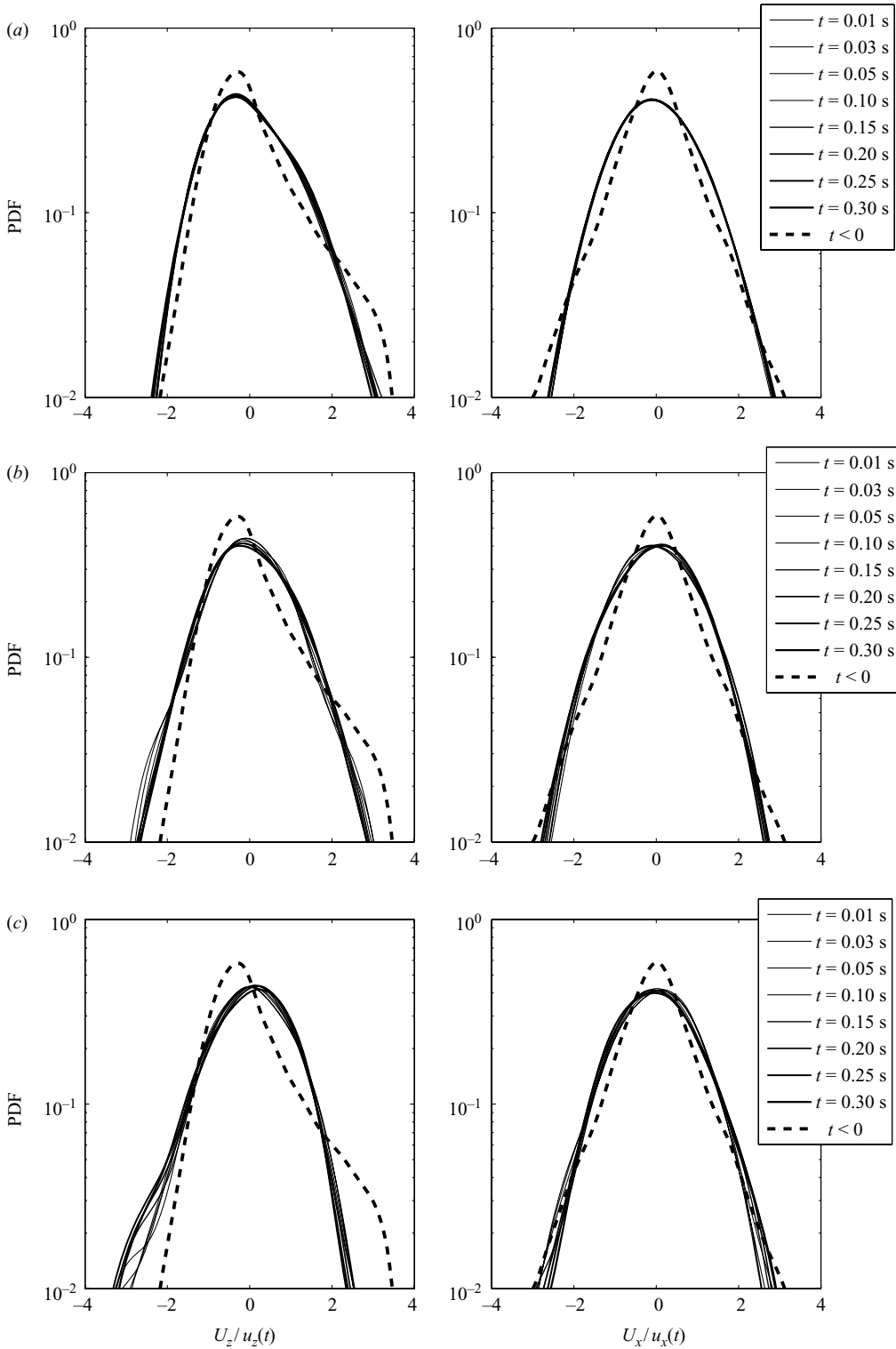
FIGURE 16. PDFs of the liquid fluctuations normalized by the standard deviations at the corresponding instants for $d = 2.5$ mm: (*a*) $\alpha = 0.0046$; (*b*) $\alpha = 0.025$; (*c*) $\alpha = 0.07$.
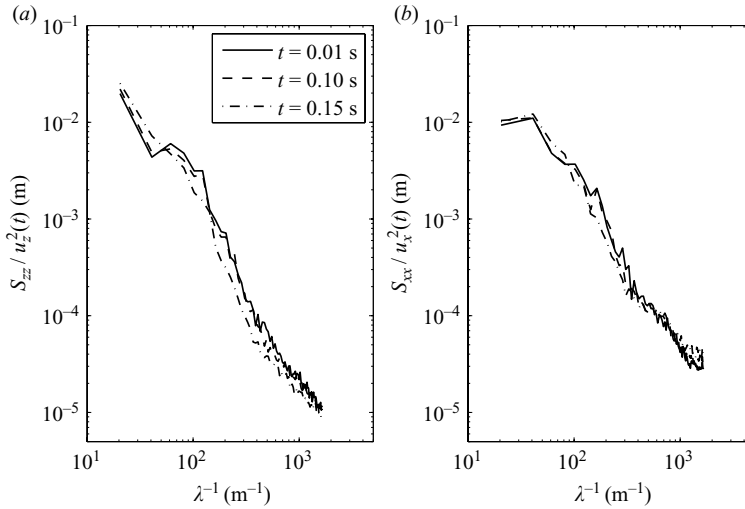
FIGURE 17. Vertical and horizontal spectra, S_{zz} and S_{xx}, of the liquid velocity fluctuations normalized by the variances at various instants t after the passage of the bubbles ($d = 2.5$ mm, $\alpha = 0.0046$).

the bubble vicinity. This is in agreement with the results of Risso & Ellingsen (2002) who showed that the conditioned PDFs corresponding to the flow in the vicinity of the bubbles was much more asymmetric than unconditioned PDFs corresponding to the flow everywhere inside the bubble swarm.

The vertical and horizontal spectra, S_{zz} and S_{xx}, have been measured using the procedure detailed in §2.3. Figure 17 presents the spectra at various instants ($0.01 \leqslant t \leqslant 0.15$ s) and shows that they do not evolve significantly during the first regime of decay, provided they are normalized by the velocity variance at the corresponding instants. For the range of wavelengths investigated, the agitation preserves the same structure while it is decaying as the distance to the bubble swarm increases. Hereinafter, all the presented spectra have been measured at $t = 0.01$ s. As for the PDFs, these spectra are measured in a region where there is no bubble and thus do not account for the flow generated in the vicinity of the bubbles, which includes the potential perturbation above and besides the bubble and a short attenuated wake behind it (see Risso & Ellingsen 2002, for a detailed description). They however describe the agitation that results from the interactions of the perturbations generated by all the bubbles. At variance with the PDFs, the present work do not provide measurements of spectra within the bubble swarm. Comparisons with results of other studies will be present in the next section after a scaling for the spectra will have been proposed. They will allow us to discuss this point.

Figure 18 collects spectra corresponding to the three bubble diameters and various volume fractions ranging from 0.004 to 0.12. Provided they are normalized by the variance of the fluctuations, the large scales of all the spectra collapse on a single master curve. For the range of parameters investigated, the large scales of the bubble-induced turbulence appear therefore to be independent of both d and α. The integral length scale Λ, roughly estimated from the value of the spectrum at the origin ($S_{zz}(0)/u_z^2$) is approximately 15 mm, indicating that most of the energy belongs to wavelengths λ much larger than the bubble diameters ($d = 1.6$–2.5 mm). Depending on λ, three different regimes can be distinguished. At the largest scales, the spectrum
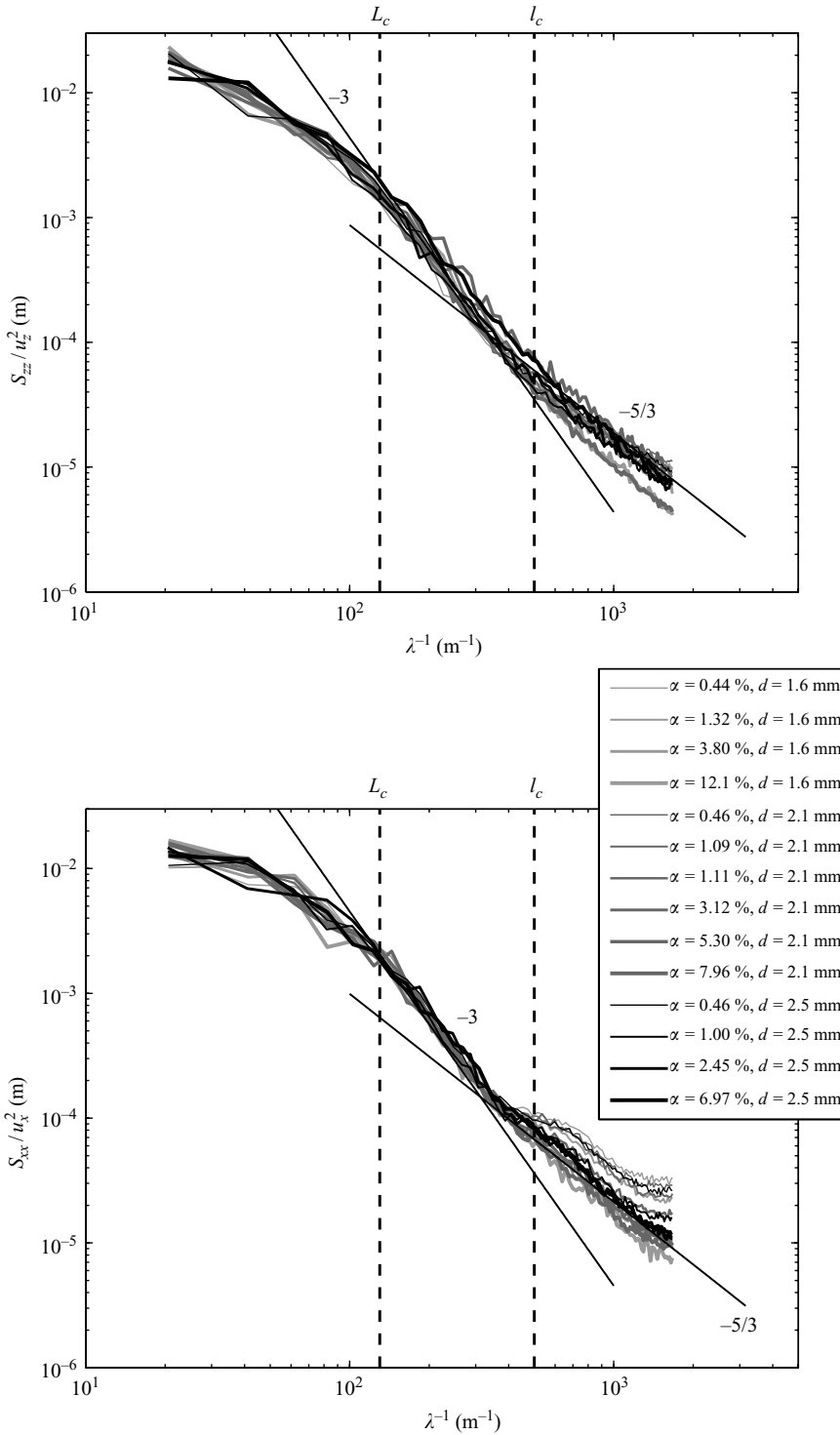
FIGURE 18. Vertical and horizontal spectra, S_{zz} and S_{xx}, of the liquid velocity fluctuations normalized by the variances for various bubble diameters d and gas volume fractions α. $L_c = 17$ mm and $l_c = 2$ mm are the upper and lower boundaries of the λ^3 range.
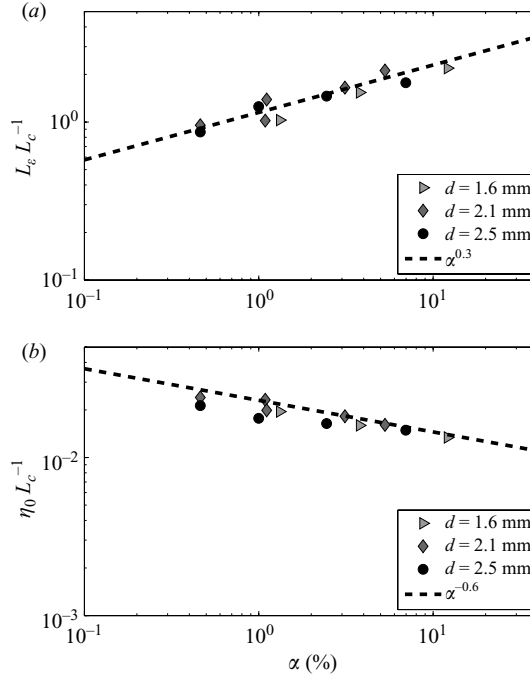
FIGURE 19. Length scales related to the dissipation rate ϵ as functions of the gas volume fraction: (a) $L_\epsilon = u^3/\epsilon$; (b) Kolmogorov microscale at time t_0 estimated from $\eta = (\nu^3/\epsilon)^{1/4}$.

shows no particular feature. For scales ranging between $L_c \approx 7.7\,\mathrm{mm}$ and $l_c \approx 2\,\mathrm{mm}$, the spectral density of energy follows a λ^3 power law. Because the upper and lower boundary, L_c and l_c, are also independent on both d and α, they are proportional to the integral length scale Λ. Moreover, since the value of L_c is of the same order to that of Λ, it can be used as an alternative length scale to characterize the large scales, with the advantage that it can be determined more accurately from the spectrum. Then, for $\lambda \leqslant l_c$, the λ^3 power law is replaced by a $\lambda^{5/3}$ power law, which probably corresponds to a classic Kolmogorov inertial subrange. At scales smaller than the resolution of the present experimental technique, the spectrum should eventually be ended by a dissipative range. To achieve the description of the spectrum, we thus need to determine the dissipation rate ϵ.

Inside the bubble swarm, the intensity of the liquid agitation is constant because the work of the drag forces exerted by the bubbles balances the energy dissipation within the liquid. Behind the bubble swarm, there is no more energy production and the kinetic energy k_e of the fluctuations starts decaying:

$$\frac{\mathrm{d}k_e}{\mathrm{d}t} = -\epsilon. \qquad (5.2)$$

Defining $u = (u_z^2 + 2u_x^2)^{1/2} = (2k_e)^{1/2}$ and combining (5.1) with (5.2) yields

$$\epsilon = \frac{u_0^2 t_0^{*2}}{t^{*3}} = \frac{u^3}{L_\epsilon}, \qquad (5.3)$$

where $L_\epsilon = u_0 t_0^*$ is independent of time. Note that the chosen instant of reference is arbitrary and has no consequence on the result; the scale L_ϵ may be calculated from any instant belonging to the first regime of decay during which the structure of the fluctuations (both PDFs and spectra) does not evolve. Figure 19(a) shows that L_ϵ is

the same for the three investigated diameters. As expected, it is of the same order of the large characteristic length scales; but in contrast with Λ and L_c, it increases with the gas volume fraction as

$$\frac{L_\epsilon}{L_c} \propto \frac{L_\epsilon}{\Lambda} \propto \alpha^{0.3}. \tag{5.4}$$

Knowing the dissipation, it is interesting to estimate the Kolmogorov microscale η in order to locate the dissipative range that probably ends the spectrum. The fact that the spectrum follows a $\lambda^{5/3}$ power law at the smallest resolved wavelengths suggests the use of the classic relation: $\eta = (\nu^3/\epsilon)^{1/4}$ ((3.2.14) in Tennekes & Lumley 1972). (Note that since the $\lambda^{5/3}$ range is preceded by a λ^3 range, we cannot be sure that the energy that cascades the inertial subrange is equal to the total dissipation; this expression might thus underpredict the value of η.) Figure 19(*b*) shows the evolution of η_0 obtained by applying this theoretical expression to the experimental values ϵ_0 of the dissipation rate at $t = 0$. The microscale η_0 is almost the same for the three bubble diameters and decreases from $2.4 \times 10^{-2} L_c$ to $1.4 \times 10^{-2} L_c$ when α increases from 0.046 to 0.12 by evolving broadly as $\alpha^{-0.6}$. This means that there is a little less than two decades between the integral scale and the cutoff wavelength of the spectrum, which is close to 0.1 mm for the cases investigated here.

It is worth noting that the agitation described here is radically different from grid turbulence. The reason lies in the fact that we are focusing on the self-preserving region that immediately follows the bubble swarm where the agitation generated by the interactions of individual bubble perturbations has not had time to reorganize yet. One could expect that farther behind the bubble swarm the agitation will relax towards isotropic turbulence as it is the case at a certain distance downstream a fixed grid. We have however no evidence of such a reorganization since the present experiments were not designed to investigate this point.

6. Summary of main results and discussion

The study of the liquid velocity fluctuations generated in a stable bubble column allowed us to determine the scaling laws for the velocity scale u and the dissipation rate ϵ of the bubble-induced turbulence. Moreover, spatial spectra measured in the region immediately following the rising homogeneous swarm shows undoubtedly a range where the spectral density of energy follows a power law of the wavelength with an exponent close to 3. This confirms the claim by Lance & Bataille (1991) that the existence of such a spectral behaviour is the signature of the bubble-induced turbulence. A question remains however open: which is the characteristic length scale of this phenomenon? Two candidates jump to mind. The bubble diameter d and the average distance between bubbles, $l_m = (\pi/6\alpha)^{1/3}d$, which is a decreasing function of the gas volume fraction. For $1.6 \leqslant d \leqslant 2.5$ mm, the spectra are independent of d and the λ^3 behaviour is observed for wavelengths larger than d. For $d = 5$ mm, Lance & Bataille (1991) observed the λ^3 behaviour only for wavelengths smaller than d. The diameter is therefore not the right scale. Then, since the measured spectra are observed to be independent of α, it can neither be l_m. By considering thoroughly the results of this work, it is however possible to find the characteristic scale.

Let us recall the scaling laws obtained for $1.6 \leqslant d \leqslant 2.5$ mm and $0.005 \leqslant \alpha \leqslant 0.1$, which relate the flow characteristics to the gas volume fraction α and the mean rise velocity of the bubbles in the limit of small volume fractions V_0. First, the mean bubble velocity $\langle V \rangle$ (figure 8) is found to scale as

$$\langle V \rangle \propto V_0 \alpha^{-0.1}, \tag{6.1}$$

whereas the bubble velocity variance (figure 10) is independent of α. Note that the validity of (6.1) is strictly restricted to the range $0.005 \leqslant \alpha \leqslant 0.1$, but its form is convenient for the present purpose. It is not clear which is the correct scaling for smaller α and from which volume fraction hydrodynamics interactions between bubbles start to play a role. On the other hand, the correlation $V_0(1 - \alpha^{0.49})$ is suitable for large volume fractions.

Concerning the liquid, the PDFs of the velocity fluctuations preserve the same shape as the gas volume fraction is increased. The knowledge of the evolution of a single characteristic velocity, say the standard deviation u, is therefore sufficient. The present measurements confirm the scaling proposed first by Risso & Ellingsen (2002),

$$u \propto V_0 \alpha^{0.4}, \tag{6.2}$$

which was confirmed here to be valid for volume fractions up to at least 0.14 thanks to the data of Larue de Tournemine (2001) .

By combining (5.3), (5.4) and (6.2) the dissipation rate ϵ can be expressed as function of the volume fraction and the integral length scale Λ (found to be independent of α):

$$\epsilon \propto \frac{V_0^3}{\Lambda} \alpha^{0.9}. \tag{6.3}$$

Another way to determine ϵ consists in considering that in a steady bubble swarm, the dissipation has to be balanced by the work of the buoyancy force:

$$\epsilon = \alpha g \langle V \rangle. \tag{6.4}$$

Now, substituting the expression of $\langle V \rangle$ from (6.1) into (6.4) yields

$$\epsilon \propto g V_0 \alpha^{0.9}. \tag{6.5}$$

Considering that the expression of ϵ given by (6.3) was obtained from the decay of the kinetic energy of the fluctuations after the passage of the bubble swarm, it is remarkable that (6.3) and (6.5) both lead to that ϵ is proportional to $\alpha^{0.9}$. Equating (6.3) and (6.5) therefore leads to an expression of Λ that is independent on α,

$$\Lambda \propto \frac{V_0^2}{g} \propto \frac{d}{C_{d0}}, \tag{6.6}$$

where $C_{d0} = 4gd/3V_0^2$ is the drag coefficient for a single rising bubble. This expression is consistent with the fact that the large scales of the spectra are independent on the volume fraction and confirms that the investigation of decaying bubble-induced turbulence was relevant to describe the structure of the agitation within the bubble swarm. Moreover, since the bubble velocity is the same for the three investigated diameters, this expression is also consistent with the fact that the spectra obtained with these three diameters were similar. It remains to check this expression for bubbles having a different rise velocity. Figure 20 compares the spectra of the present work to those obtained by Lance & Bataille (1991) and Larue de Tournemine (2001) after normalization by using d/C_{d0} as characteristic length scale. Note that it is only in our case that the spectrum S_{xx} of the horizontal velocity component is available and that it is similar to the spectrum S_{zz} of the vertical velocity component. For the present results ($1.6 \leqslant d \leqslant 2.5$ mm) and those of Larue de Tournemine (2001) ($d = 1.75$ mm), $d/Cd_0 = 8.6$ mm. In the case of Lance & Bataille (1991), the bubbles are about twice larger ($d = 5$ mm, $V_0 = 0.24$ m s^{-1}), but the length scale, $d/Cd_0 = 4.4$ mm, is about twice smaller.
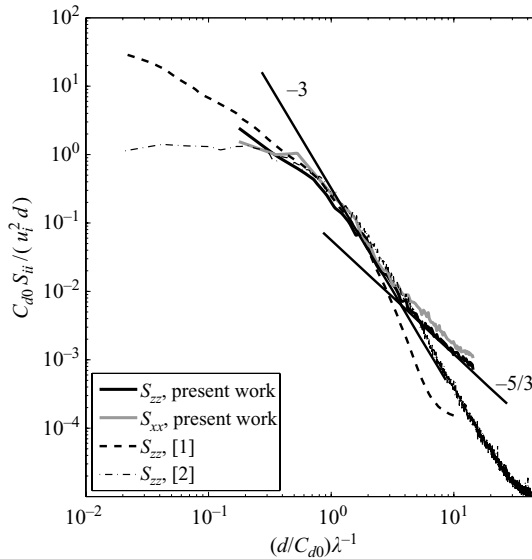
FIGURE 20. Spectra normalized by using the variance and the characteristic length scale d/C_{d0}: solid lines, present study with $1.6\,\text{mm} \leqslant d \leqslant 2.5\,\text{mm}$; [1] Lance & Bataille (1991) with $d = 5\,\text{mm}$; [2] Larue de Tournemine (2001) with $d = 1.75\,\text{mm}$.

On the one hand, we see that all the spectra match well at large scales and, in particular, the beginning of the λ^3 range is observed for the same wavelength, $L_c \approx d/Cd_0$ for all bubble sizes and for both the vertical and the horizontal velocity components. Firstly, the agreement with the results of Larue de Tournemine (2001), which were obtained for a similar bubble size but within the bubble swarm, shows that the large scales are dominated by wake interactions and are not significantly influenced by the absence of the flow perturbation in the close vicinity of the bubbles. We can therefore conclude that the spectra measured just behind the bubble swarm describe well the scales larger than l_c. Secondly, the agreement with the results of Lance & Bataille (1991), which were obtained for larger bubbles, confirms the validity of the scaling (6.6).

On the other hand, for wavelengths smaller than $l_c \approx L_c/4$, the λ^3 range is replaced by a $\lambda^{5/3}$ range in the present spectra, whereas the λ^3 range extends up to the smallest resolved scale in the spectra of Larue de Tournemine (2001) or is even prolonged by a steeper evolution in the case of Lance & Bataille (1991). Some experimental conditions used by Lance & Bataille (1991) and Larue de Tournemine (2001) differ from ours and may cause the observed discrepancies at small scales: (i) they investigated bubbles rising in a moving fluid so a certain amount of shear-induced turbulence is present; (ii) they used time series of single-point measurements that were interpolated; (iii) they computed time spectra that were changed into spatial spectra by using the Taylor hypothesis. It is also possible that the existence of a $\lambda^{5/3}$, which is probably the signature of a return to isotropy at small scales, can only be observed in the absence of the strong perturbations generated in the vicinity of the bubbles; in that case, the small scales observed behind the bubble swarm would differ from those measured within it. We are nevertheless not able to propose a definitive interpretation of the differences with our results.

All together, the self-similar shape of the PDFs, the normalized spectra for both velocity components and relations (6.2), (6.3) and (6.6) provide an almost complete description of the dynamics of the liquid agitation induced by bubbles rising in water in the absence of any other cause of fluctuations, at least for gas volume fractions ranging from 0.005 to 0.14 and diameters from 1.5 to 5 mm. The next challenge will be to understand the physical mechanisms responsible for the self-similarity of the PDFs and the λ^3 range in the spectra. Concerning the PDFs, we already know that the non-Gaussian shape as well as the anisotropy is due to the flow in the vicinity of each bubble since the fluctuations recover isotropy and Gaussian distribution just behind the bubble swarm. Concerning the λ^3 range, the present results indicates that it implies hydrodynamic interactions between the flow disturbances induced by individual bubbles since it was observed for wavelengths much larger than the bubble diameter. The interpretation proposed by Lance & Bataille (1991), which was based on the assumption of an equilibrium between production and dissipation within each individual wake, is therefore invalidated. Future models for bubble-induced agitation have to generate fluctuations at scales of order d/Cd_0 whatever the value of d.

REFERENCES

ABBAS, M. & CLIMENT, E. 2006 Dynamics of bidisperse suspensions under stokes flows: linear shear flow and sedimentation. *Phys. Fluids* **18**, 121504.

CALFISH, R. E. & LUKE, H. C. 1985 Variance in the sedimentation speed of a suspension. *Phys. Fluids* **28**, 759–760.

CARTELLIER, A. & RIVIÈRE, R. 2001 Bubble-induced agitation and microstructure in uniform bubbly flows at small to moderate particle Reynolds numbers. *Phys. Fluids* **13**, 2165–2181.

CID, E. & GARDELLE, F. 2005 *Manuel d'utilisation du logiciel PIVis*. Institut de Mécanique des Fluides de Toulouse.

EAMES, I., ROIG, V., HUNT, J. C. R. & BELCHER, S. E. 2004 Vorticity annihilation and inviscid blocking in multibody flows. In *NATO Advanced Study Institute: Flow and Transport Processes in Complex Obstructed Geometries: From Cities and Vegetative Canopies to Industrial Problems*, Kiev, Ukraine.

ELLINGSEN, K. & RISSO, F. 2001 On the rise of an ellipsoidal bubble in water: oscillatory paths and liquid-induced velocity. *J. Fluid Mech.* **440**, 235–268.

GARNIER, C., LANCE, M. & MARIÉ, J. L. 2002 Measurement of local flow characteristics in buoyancy-driven bubbly flow at high void fraction. *Exp. Therm. Fluid Sci.* **26**, 811–815.

HUNT, J. C. R. & EAMES, I. 2002 The disappearance of laminar and turbulent wakes in complex flows. *J. Fluid Mech.* **457**, 111–132.

KIAMBI, S. L., DUQUENNE, A.-M., DUPONT, J.-B., COLIN, C., RISSO, F. & DELMAS, H. 2003 Measurements of bubble characteristics: comparison between double optical probe and imaging. *Can. J. Ch. Engng* **81**.

KOCH, D. L. 1993 Hydrodynamic diffusion in dilute sedimenting suspensions at moderate Reynolds numbers. *Phys. Fluids* A **5**, 1141–1155.

LANCE, M. & BATAILLE, J. 1991 Turbulence in the liquid phase of a uniform bubbly air–water flow. *J. Fluid Mech.* **222**, 95–118.

LARUE DE TOURNEMINE, A. 2001 Etude expérimentale de l'effet du taux de vide en écoulement diphasique à bulles. PhD thesis, Institut National Polytechnique de Toulouse, France.

MANASSEH, R., RIBOUX, G. & RISSO, F. 2008 Sound generation on bubble coalescence following detachment. *Intl J. Multiph. Flow* **34**, 938–949.

MARTINEZ-MERCADO, J., PALACIOS-MORALES, C. & ZENIT, R. 2007 Measurement of pseudo-turbulence intensity in mono-dispersed bubbly liquids. *Phys. Fluids* **19**, 103302.

MAXWORTHY, T., GNANN, C., KURTEN, M. & DURST, F. 1996 Experiments on the rise of air bubbles in clean viscous liquids. *J. Fluid Mech.* **321**, 421–441.

PARTHASARATHY, R. N. & FAETH, G. M. 1990 Turbulence modulation in homogeneous dilute particle-laden flows. *J. Fluid Mech.* **220**, 485–514.

RENSEN, J., LUTHER, S. & LOHSE, A. 2005 The effect of bubbles on developed turbulence. *J. Fluid Mech.* **538**, 153–187.

RISSO, F. & ELLINGSEN, K. 2002 Velocity fluctuations in homogeneous dilute dispersion of high-Reynolds-number rising bubbles. *J. Fluid Mech.* **453**, 395–410.

RISSO, F., ROIG, V., AMOURA, Z., RIBOUX, G. & BILLET, A.-M. 2008 Wake attenuation in large Reynolds number dispersed two-phase flows. *Phil. Trans. R. Soc.* A **366**, 2177–2190.

ROIG, V. & LARUE DE TOURNEMINE, A. 2007 Measurement of interstitial velocity of homogeneous bubbly flows at low to moderate void fraction. *J. Fluid Mech.* **572**, 87–110.

TENNEKES, H. & LUMLEY, J. L. 1972 *A First Course in Turbulence*. MIT Press.

WESTERWEEL, J. & SCARANO, F. 2005 Universal outlier detection for PIV data. *Exp. Fluids* **39**, 1096–1100.

WHITE, B. L. & NEPF, H. M. 2003 Scalar transport in random cylinder arrays at moderate Reynolds number. *J. Fluid Mech.* **487**, 43–79.

ZENIT, R., KOCH, D. L. & SANGANI, A. S. 2001 Measurements of the average properties of a suspension of bubbles rising in a vertical channel. *J. Fluid Mech.* **429**, 307–342.